

Imperfection-Insensitive Axially Loaded Cylindrical Shells

Xin Ning^{*} and Sergio Pellegrino[†]

California Institute of Technology, Pasadena, CA 91125

The high efficiency of monocoque cylindrical shells in carrying axial loads is curtailed by their extreme sensitivity to imperfections. For practical applications, this issue has been alleviated by introducing closely stiffened shells which, however, require expensive manufacturing. Here we present an alternative approach that provides a fundamentally different solution. We design symmetry-breaking wavy cylindrical shells that avoid imperfection sensitivity. Their cross-section is formulated by NURBS interpolation on control points whose positions are optimized by evolutionary algorithms. We have applied our approach to both isotropic and orthotropic shells and have also constructed optimized composite wavy shells and measured their imperfections and experimental buckling loads. Through these experiments we have confirmed that optimally designed wavy shells are imperfection-insensitive. We have studied the mass efficiency of these new shells and found them to be more efficient than even a perfect circular cylindrical shell and most stiffened cylindrical shells.

Nomenclature

a	imperfection amplitude, μm
A	surface area of shell, in^2
e_p	normal distance between p^{th} measured point and perfect shell
E	Young's modulus, GPa or psi
f_{peak}	peak spatial frequency, $(1/\text{m})$
G	shear modulus, GPa
L	length of cylindrical shell, mm
m	wavelength parameter of imperfections
M	number of measurement points
N	number of control points
N_x	critical stress resultant, lb/in
P	axial load
$P_{\text{per}}, P_{\text{imp}}$	buckling loads of perfect and imperfect shells
P_{CL}	classical buckling load for circular cylindrical shell
R	mid-thickness radius of circular cylindrical shell, mm or in
R_z	rotation w.r.t z -axis
t	shell thickness, μm
T_x, T_y	translations in x and y directions, mm
W	total weight of shell, lb
w_i	displacement of i^{th} control point, mm
$w_{q,i}$	radial coordinate of i^{th} control point in q^{th} quarter of shell, mm
x	axial coordinate, mm
γ	knockdown factor
δ, δ_a	lateral and axial displacement components
$\Delta V, \delta^i V$	change of potential energy and i^{th} order term

^{*}Graduate Student. Graduate Aerospace Laboratories, California Institute of Technology, 1200 E. California Blvd. MC 105-50. e-mail xning@caltech.edu

[†]Joyce and Kent Kresa Professor of Aeronautics and Professor of Civil Engineering, Graduate Aerospace Laboratories, California Institute of Technology, 1200 E. California Blvd. MC 301-46. AIAA Fellow. e-mail sergiop@caltech.edu

ε_x	strain in axial direction
λ	ratio of applied load to theoretical buckling load
$\theta_{q,i}$	angular coordinate of i^{th} control point in q^{th} quarter of shell
λ_{per}	ratio of buckling load of perfect shell to theoretical buckling load
λ_{imp}	ratio of buckling load of imperfect shell to buckling load of perfect shell
μ	ratio of imperfection amplitude to shell thickness
ν	Poisson's ratio
ξ	efficiency of cylindrical shells
ξ_a	efficiency of perfect aluminum circular cylindrical shells
ρ	density, lb/in ³
Φ_{cr}	critical buckling mode

I. Introduction

Large discrepancies between analytically predicted and experimentally measured buckling loads for monocoque cylindrical shells were first observed in the 1930's, leading to the now widely known fact that thin cylindrical shells under axial compression may buckle at loads as low as 20% of the classical value [1]. The generally accepted approach to the design of axially compressed monocoque cylindrical shells against buckling is to use empirically defined knockdown factors, in which shell structures are designed to have large theoretical buckling loads to ensure that, when the knockdown factor is applied, the design requirements are still met [2]. As a result, the high efficiency of monocoque cylindrical shells in carrying axial loads is curtailed by their extreme sensitivity to geometric imperfections, boundary conditions, loading, etc., and an alternative structural architecture, closely stiffened shells, i.e., cylindrical shells reinforced by stringers/corrugations and rings, is used in applications requiring the highest structural efficiency. This alternative architecture is currently established as the premiere efficient aerospace structure [3] and is widely used for lightness and extreme efficiency.

Instead of this established approach, we follow Ramm and co-workers [4–6] and compute optimal cross-sectional shapes for monocoque shells in order to maximize the critical buckling load and at the same time reduce the imperfection sensitivity. This approach produces shells with a novel shape and differs fundamentally from the knockdown-factor method. The shells obtained from the knockdown-factor method are still imperfection-sensitive, although the use of buckling loads reduced by application of a knockdown factor allows them to meet any prescribed design requirements.

Structural optimization is a powerful tool to obtain the maximum critical buckling load but it normally leads towards designs that are highly imperfection-sensitive, see for example [7]. This serious drawback was addressed by Reitinger, Bletzinger and Ramm [5,6] who introduced the critical buckling loads of both perfect and imperfect structures into the optimization process to obtain structures that have a high buckling load and at the same time are also imperfection insensitive. This method was previously applied only to thin-shell concrete roofs, but its applicability to general structures motivates us to explore the design of imperfection-insensitive cylindrical shells with maximal critical buckling loads.

The paper is organized as follows. In Section II a brief literature review of influence of imperfections on cylindrical shells is first presented, followed by current approaches to design of cylindrical shells against buckling. We then present Ramm's method to reduce imperfection-sensitivity. With this background, in Section III we present the methodology used to obtain imperfection-insensitive cylindrical shells. This methodology is then implemented in Section IV, in which designs of isotropic and composite cylindrical shells are presented. We studies the effects of design variables, and the results are presented in Section V. Section VI provides the techniques of constructing the composite shell designed in Section IV, as well as the methods of measuring imperfections. Test results are then presented. The experimental results are discussed in Section VII. Section VIII concludes the paper.

II. Background

This section provides a brief review of the influence of initial imperfections on cylindrical shells, current approaches to the design of cylindrical shells against buckling and Ramm's method to reduce imperfection-sensitivity in thin-shell structures. A description of the Aster shell, which was based on a cross-section

intuitively designed to avoid buckling, is provided.

A. Effects of Imperfections

There is a huge body of literature on this subject, and extensive reviews have been compiled by several authors, see Refs [1, 8, 9]. Here we focus only the essential background to the approach proposed in the present study.

The first major contribution to the present understanding of the effects of initial imperfections on the buckling of circular cylindrical shells was made by von Kármán and Tsien [10] who analyzed the postbuckling equilibrium of axially compressed cylindrical shells. Fig. 1, showing a sharply dropping second equilibrium path, suggests that an initially imperfect shell buckles at the limit point B rather than the bifurcation point A. Donnell and Wan [11] analyzed initially imperfect cylindrical shells and obtained equilibrium paths with the form of the dash line in Fig. 1. Koiter analyzed the influence of axisymmetric imperfections [12] and the results are summarized in Fig. 2, showing that imperfections with even a small amplitude can dramatically reduce the buckling load. In this analysis, the imperfection was restricted to the form:

$$a = -\mu t \cos \frac{2mx}{R} \quad (1)$$

where m is a wavelength parameter, t the thickness of the shell, and R and x the radius and axial coordinate, respectively. The imperfection wavelength m taken in Koiter's analysis leads to an imperfection which coincides with the axisymmetric buckling mode of a perfect cylindrical shell.

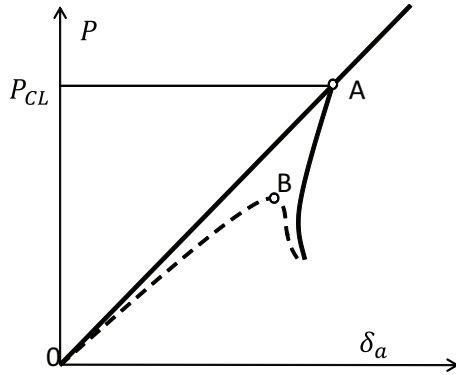


Figure 1: Equilibrium paths for axially compressed perfect (solid line) and imperfect (dash line) cylindrical shells. P and P_{CL} are the compressive load and the classical critical buckling load, respectively, and δ_a denotes the axial end-shortening.

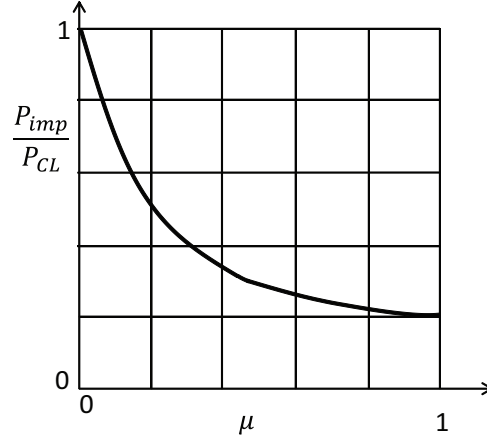


Figure 2: Influence of imperfection amplitude μ (ratio of imperfection amplitude to shell thickness) on buckling load P_{imp} of imperfect shells.

A more general analysis of the influence of initial imperfections had been presented by Koiter [13]. It was based on an analysis of the potential energy of the loaded structure in a general buckled equilibrium configuration, thus it is applicable to asymmetric imperfections and shells of arbitrary shape [1]. The change in potential energy of a perfect structure is written as:

$$\Delta V = \frac{1}{2!} \delta^2 V + \frac{1}{3!} \delta^3 V + \frac{1}{4!} \delta^4 V \quad (2)$$

The secondary equilibrium path is obtained by application of the stationary potential energy criterion to the above expression. The Koiter theory provides an approximate solution to the second equilibrium path for a perfect structure:

$$\lambda \equiv \frac{P}{P_{CL}} = 1 + a_1 \delta + a_2 \delta^2 + \dots \quad (3)$$

where P and P_{CL} , respectively, are the applied load and the classical bifurcation load; a_1 , a_2 , ... are constants and δ is a measure of the lateral displacement amplitude. The results are shown as solid lines in Fig. 3. In case I $a_1 \neq 0$ and for small values of δ the secondary equilibrium path is approximately a straight line. For the other cases $a_1 = 0$, resulting in parabolic secondary equilibrium paths, and $a_2 < 0$ for case II and $a_2 > 0$ for case III.

The corresponding equilibrium paths for imperfect structures are shown by dash lines in Fig. 3. Cases I and II represent structures that are *sensitive to imperfections*, because the buckling loads of the imperfect structures ($\lambda_{imp,-}$ for case I and $\lambda_{imp,\pm}$ for case II) are lower than 1. Fig. 3 indicates that in case I the sign of the imperfection may lead to different types of imperfection-sensitivity.

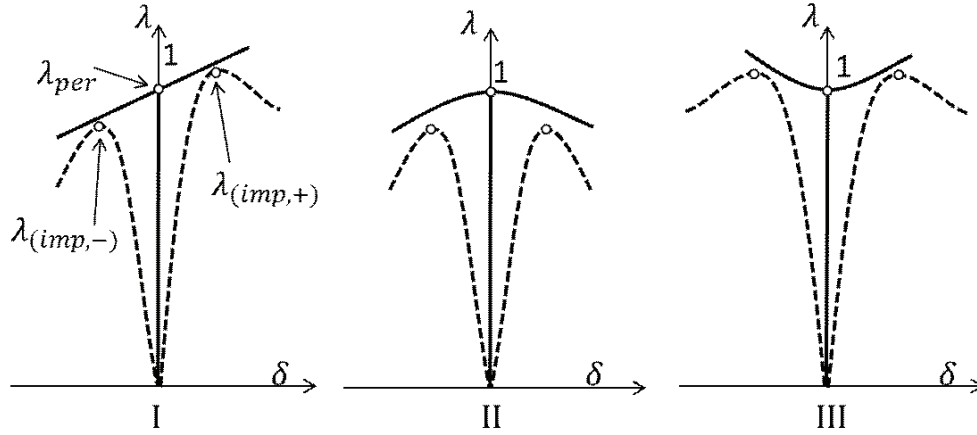


Figure 3: Three types of post-buckling equilibrium paths for perfect and imperfect structures, from [1] and [13]. $\lambda_{per} = 1$ and $\lambda_{imp,\pm}$ are ratios between buckling loads of imperfect structures with positive/negative imperfections and perfect structures.

B. Design of Cylindrical Shells Against Buckling

The generally accepted approach to the design of axially compressed monocoque cylindrical shells against buckling is to adopt the *knockdown-factor method* to account for the reduction of buckling load due to imperfections. The actual buckling load of a cylindrical shell is estimated from:

$$P_{imp} = \gamma P_{per} \quad (4)$$

where P_{imp} and P_{per} are the buckling loads of the actual, i.e. imperfect shell and the corresponding perfect shell, respectively, and γ is the knockdown factor. P_{per} is given by the classical formula:

$$P_{per} = \frac{2\pi E t^2}{\sqrt{3(1-\nu^2)}} \quad (5)$$

where E , ν and t are the Young's modulus, Poisson's ratio and shell thickness, respectively.

A widely used expression for the knockdown factor of axially compressed cylindrical shells is the empirical curve provided in the NASA report [14] and shown in Fig. 4. Given the radius to thickness ratio R/t , the empirical curve provides a lower bound to the experimentally derived knockdown factors and hence can be used to predict the experimental buckling load from Eq. 4. Designs obtained from this approach have to achieve a theoretical buckling load P_{per} high enough that the reduced buckling load P_{imp} satisfies the design requirements. A fundamental aspect of the knockdown-factor design method is that it still produces highly imperfection-sensitive shells.

The empirical knockdown factor in Fig. 4 was derived from many tests conducted over a long period of time and recently it has been argued that the manufacturing, loading and boundary conditions for all the shells that were tested are not sufficiently well-known to provide a rational basis for modern design. Also, most tests were conducted on metallic shells, whereas contemporary structures such as fiber-reinforced composite shells were not addressed [2,15]. The knockdown-factor approach tends to provide overly conservative designs because it always assumes the worst imperfections which may not be a reasonable representation for a specific shell.

An emerging alternative approach is to obtain for each specific manufacturing process a signature of the manufacturing imperfections, i.e. a statistical representation of the geometric imperfections [2, 16, 17]. In this approach the geometric imperfections are measured, and the mean imperfection shape and standard

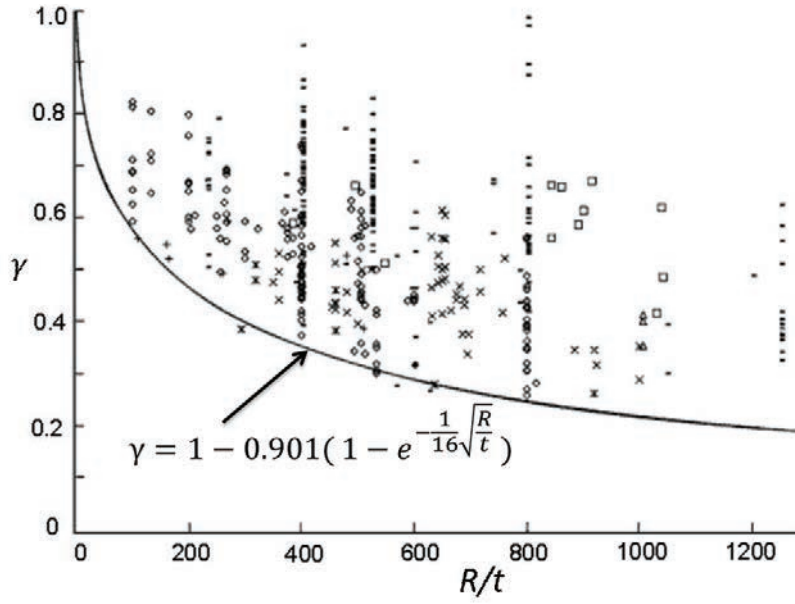


Figure 4: Experimental knockdown factor of cylindrical shells under axial compression and the empirical curve for the knockdown factor, $\gamma = 1 - 0.901 \left(1 - e^{-\frac{1}{16} \sqrt{\frac{R}{t}}} \right)$, plotted versus the radius to thickness ratio, R/t . [14]

deviation are obtained as characteristics of the corresponding manufacturing process. This characteristic imperfection is then applied in the analysis to accurately predict the experimental buckling load. With the information established from measured imperfections, this approach can provide reliable design criteria for shell buckling that are not overly conservative [17].

Stiffened cylindrical shells were introduced to alleviate the imperfection-sensitivity of monocoque shells. Due to the many different potential configurations for the stiffeners, a comparison in terms of knockdown factors alone is not very meaningful. However it should be noted that experiments on 12 longitudinally stiffened cylindrical shells with internal or external, integral or Z-stiffeners obtained knockdown factors ranging from 0.7 to 0.95, indicating a much lower imperfection-sensitivity than monocoque cylindrical shells [18].

Instead of using the knockdown factor, the buckling performance of monocoque, stiffened, and all other kinds of cylindrical shells can be compared by considering the weight and load structural indices [19–21], defined as follows:

$$\begin{aligned} \text{Weight index : } & \frac{W}{AR} \\ \text{Load index : } & \frac{N_x}{R} \end{aligned} \quad (6)$$

where W , A , R are the total weight of the shell, the area and radius of the cylinder, respectively, and N_x denotes the critical buckling stress resultant. For circular cylindrical shells, the relation between weight and load indices is:

$$\frac{W}{AR} = \rho \left(\frac{\sqrt{3(1-\nu^2)} N_x}{\gamma E} \frac{1}{R} \right)^{\frac{1}{2}} \quad (7)$$

Note that the two performance indices are dimensional, this is the form commonly used by shell designers.

In addition to reducing imperfection-sensitivity, stiffened cylindrical shells are known to be mass efficient. This is seen in the plot in Fig. 5. Shells closer to the right-bottom corner of the chart can carry larger load with less material and therefore have higher efficiency. The inclined straight line in the figure represents the performance of perfect monocoque circular cylindrical shells ($\gamma = 1$); the horizontal line corresponds

to lightly-loaded shells which are subject to a minimum thickness constraints. The chart shows that most stiffened cylindrical shells have even higher efficiency than even the perfect monocoque circular cylindrical shells.

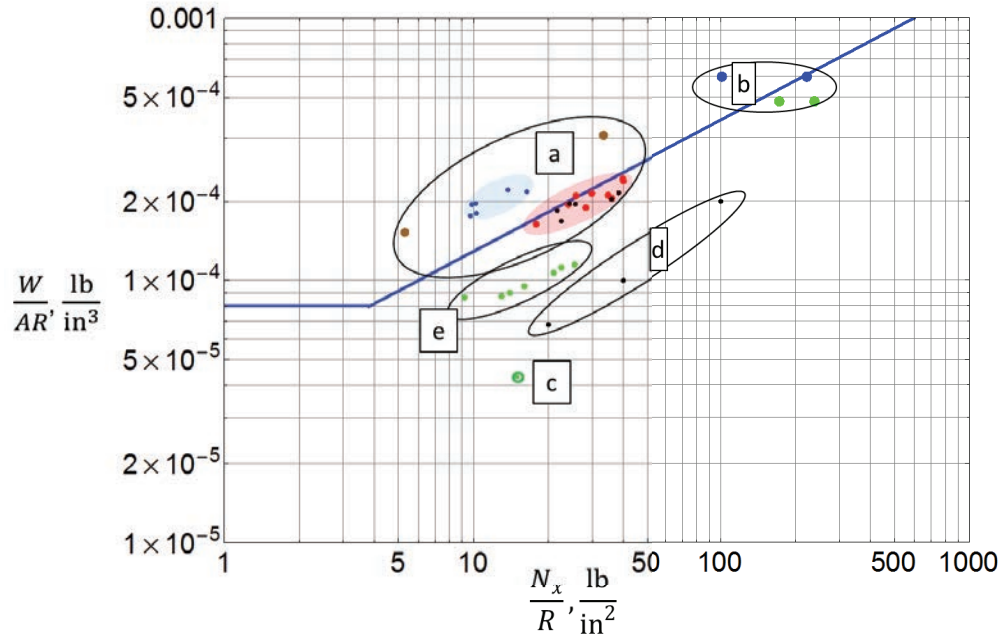


Figure 5: Performance metrics chart showing available data for stiffened cylindrical shells, provided by Dr M.M. Mikulas). The shells in groups a, b, c and d are shown in Fig. 6. Group e corresponds to z-stiffened shells.

It should also be noted that, despite their many advantages, stiffened cylindrical shells require complex manufacturing processes. Machining from thicker stock and special forgings are the main manufacturing methods [3] and these processes are expensive. In 1986 prices on the order of \$3,500 for a 320 mm diameter steel shell stiffened in one direction and about \$15,000 for a similar orthogonally stiffened shell were quoted [3, 22].

An alternative to stiffened shells was proposed in 1991 by Jullien and Araar; their intuitive design of an imperfection-insensitive cylindrical shells was called “Aster” shell [23]. They argued that under axial compression inward imperfections in a cylindrical shell become amplified, whereas outward imperfections maintain a constant amplitude. Based on this consideration, they considered a sinusoidally varying deviation from the circular cross-section and took the mirror image of all concave parts of this geometry to obtain a shape that is everywhere convex apart from symmetrically distributed localized kinks, as shown in Fig. 7. This approach can be considered a precursor of the present study.

C. Ramm’s Method to Reduce Imperfection-Sensitivity

Ramm and co-workers proposed a topology optimization method for thin shell structures and used it to optimize simply-supported arches under a concentrated load [5], stiffened panels and free-form shells [6]. Instead of considering only the buckling load of perfect trial structures, as in conventional structural optimization, Ramm’s method considered both perfect and imperfect structures in evaluating the objective function. This fundamental difference allows Ramm’s method to avoid converging towards highly imperfection-sensitive structures.

The method consists of four steps linked in an optimization loop, as shown in Fig. 8. First, the critical buckling load (P_{per}) and the critical buckling mode (ϕ_{cr}) are calculated for the perfect structure. Second, the critical buckling mode scaled by a prescribed amplitude is adopted as imperfection shape and it is then superposed to the perfect geometry to create an imperfect shape. Third, the critical buckling load (P_{imp}) for the imperfect structure is calculated. Finally, the lower of P_{per} and P_{imp} is chosen as the value of the objective function.

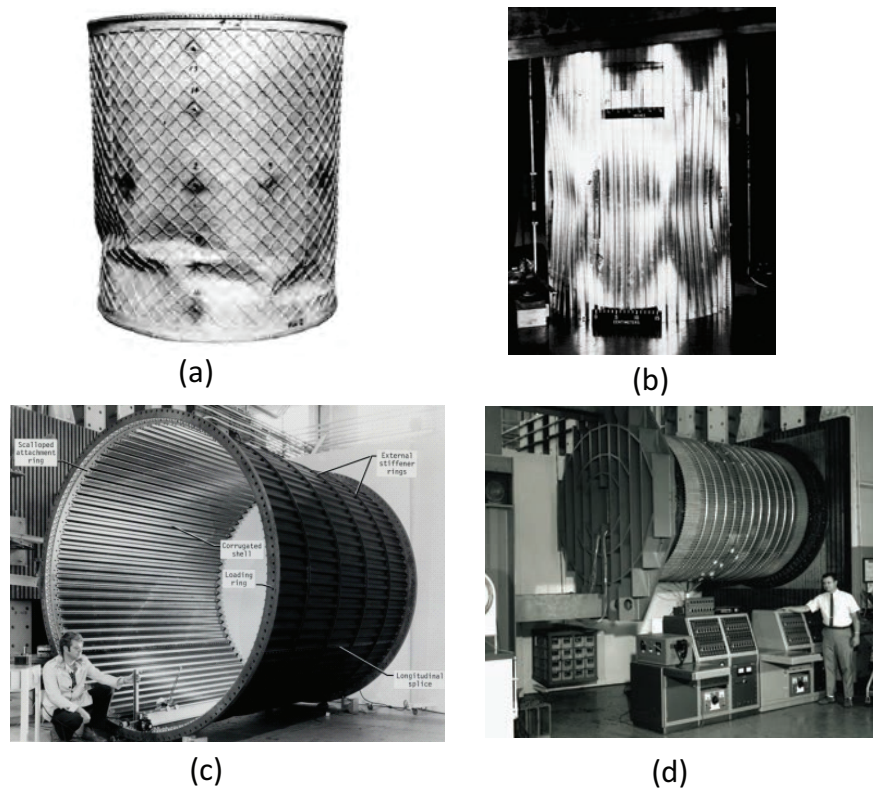


Figure 6: Stiffened shells shown in Fig. 5.

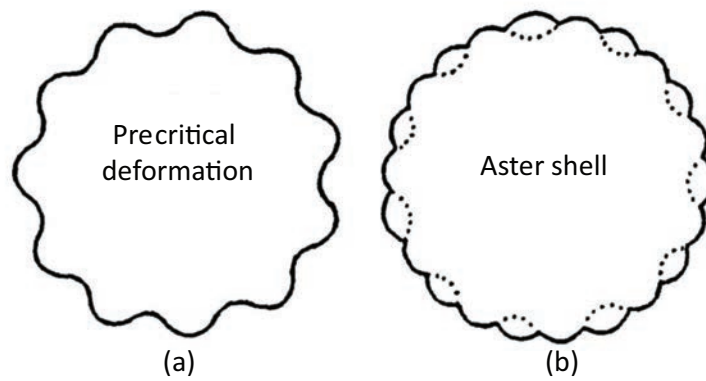


Figure 7: Cross-section of (a) precritical deformation mode of circular cylindrical shell and (b) Aster shell. [23]

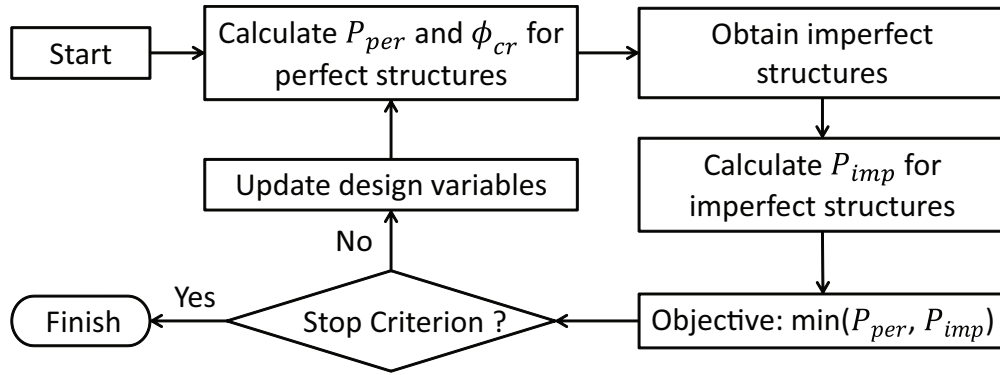


Figure 8: Flow chart of Ramm's Method.

Reference [6] studies the optimal shape of a four-point supported shell structure under dead load, see Fig. 9 [4, 6]. The results of a standard optimization that considers only perfect structures are shown in the upper-left part of the figure, where it can be seen that the buckling load factor, defined as the ratio of buckling load to applied dead load, is 84.3. However, in this case there is significant imperfection-sensitivity, as shown by a calculation of several shape-imperfect structures which have a buckling load factor as low as 54.3. An alternative optimization, based on both perfect and imperfect structures, has also been carried out and the results are shown in the lower-left part of the figure. In this case the buckling load factor is only reduced to 74.0 from 83.1, indicating a reduced imperfection-sensitivity.

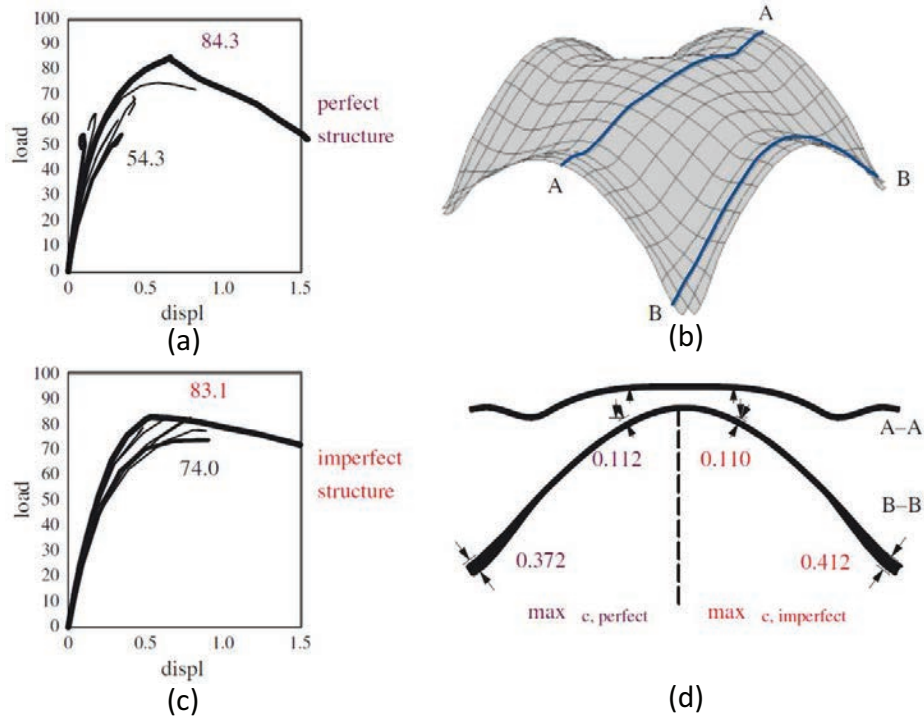


Figure 9: Application of Ramm's method. (a) Buckling loads of optimized shell based on optimization of perfect shell geometry only. (b) Shape of optimized shell. (c) Buckling loads of optimized shell based on optimization that considered also imperfect shells. (d) Cross-sectional shapes of perfect and imperfect shells.

III. Methodology

We adopt Ramm’s method to search for the cross-sectional shape of an imperfection-insensitive cylindrical shell with maximal buckling load, to optimize the shape of cylindrical shells. We first present the methodology to parameterize the shape of the cross-section and formulate the design problem, and then present the implementation of the design process.

A. Parametrization of Cross-section

As discussed in Section II, using corrugated cylindrical shells rather than circular cross-section shells can increase both the buckling load and the resistance to imperfections. The Aster shell, which has a convex lobed surface, is essentially a corrugated shell. The advantages of corrugated cross-sections inspired us to explore more general cross-sectional shapes and thus we introduce the concept of the “Wavy Shell”, shown in Fig. 10 (a). The cross-section of wavy shell is uniform in the axial direction, because axially non-uniform cross-sections will have to carry shear and possibly even bending under axial compression which may decrease the axial stiffness. The shape of the cross-section is defined by a series of controls points; a 3rd degree NURBS (Non-Uniform Rational B-Spline) is adopted to create a smooth curve through the control points. NURBS can offer the ability to exactly describe a wide range of objects that cannot be exactly represented by polynomials [24]. The order of NURBS is typically 3 (cubic) which gives C^2 continuity, i.e. the curvature varies smoothly.

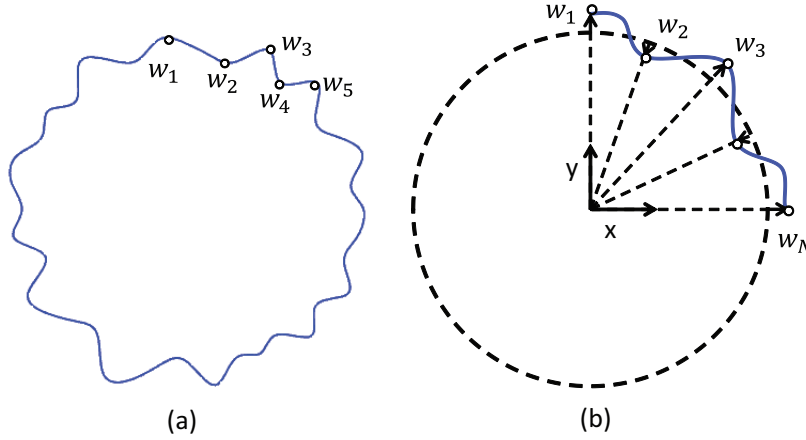


Figure 10: (a) Schematic of generic wavy shell showing also the control points. w_i , $i = 1, 2, 3, \dots$ denote the radial displacements of the control points. (b) Mirror-symmetric wavy shell with N equally spaced control points. The dash line is the reference circular shell.

For the present study we introduce two main geometric constraints to narrow the design space. First, the shell is symmetric with respect to the x - and y -axes, see Fig. 10 (b), therefore we only need to optimize the control points in a quarter of the shell. Second, the control points are equally spaced circumferentially and are only allowed to move radially from the reference circle, which is defined as the radius of the wavy shell. The maximum possible displacements for all controls points are equal and fixed during the optimization. Positive displacements represent control points lying outside the circle. Thus the parametrization of the cross-section of the wavy shell is given by the displacements of N control points located in the first quadrant.

B. Formulation of Optimization Problem

In Ramm’s method the smallest of the buckling loads of the perfect and imperfect structures is assigned as the value of the objective function. The geometry of the imperfect structure is obtained by superposing imperfections onto the perfect structure. A reasonable choice for the imperfection shape is the critical buckling mode. We assume that this choice leads to a larger reduction of buckling load than any other imperfections with the same amplitude as the critical buckling-mode imperfection. There may well be more refined approaches, based on other forms of imperfections that would give a lower buckling load. However,

this assumption is a common assumption to estimate a lower bound on the actual buckling load, see for example [2, 17]. Fig. 11 shows a schematic representation of this process.

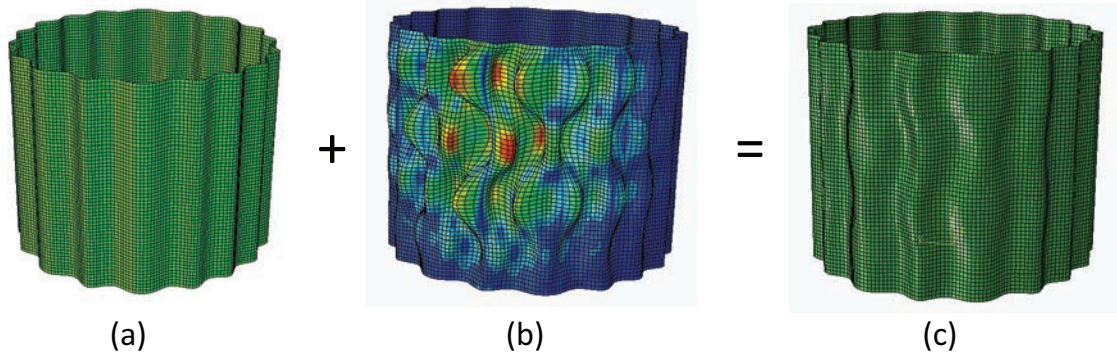


Figure 11: (a) Perfect wavy shell. (b) Imperfection shape based on critical buckling mode. (c) Imperfect shell obtained by superposing imperfection onto perfect shell.

Similar to the shape of imperfections, the real amplitude of the imperfection also depends on the quality of manufacturing. Fig. 2 shows that imperfection amplitudes on the order of the shell thickness reduce the buckling load to as low as 20% of the theoretical value. Thus, the amplitude of imperfections used in our design is chosen to be equal to the shell thickness.

As discussed in the previous section, different signs of imperfections may lead to different types of imperfection-sensitivity. Therefore, shells with both positive and negative amplitudes of imperfections are considered in the optimization. With these assumptions, we expect a reasonable **estimate** of the buckling loads of imperfect shells, provided that the actual imperfection amplitude does not exceed one shell thickness.

The optimization problem can be formulated as follows:

$$\begin{aligned}
 &\text{Maximize : } \min (P_{per}, P_{imp,+}, P_{imp,-}) \\
 &\text{Subject to : } (1) |w_i| \leq w_{max}, i = 1, 2, 3, \dots, N \\
 &\quad (2) \text{ Control points equally spaced in circumferential direction.} \\
 &\quad (3) \text{ Control points move only radially.} \\
 &\quad (4) \text{ Cylindrical shell is symmetric with respect to x and y axes.} \\
 &\quad (5) \text{ Cylindrical shell has uniform cross-section in axial direction.}
 \end{aligned} \tag{8}$$

where P_{perf} and $P_{imp,\pm}$ are the critical buckling loads for perfect and imperfect structures, respectively. The displacements of control points w_i are bounded by a prescribed w_{max} so that excessive curvature of the cross-section is avoided.

C. Optimization Implementation

We have developed a MATLAB script that connects CAD software, finite-element analysis software and an optimizer to implement the complete optimization cycle. Rhino 3D, a NURBS-based CAD software, was adopted to create CAD files for the finite element analysis. Next, the software Abaqus/CAE was used to read the files generated by Rhino 3D and evaluate the structural performance. The critical buckling mode was obtained from an eigenvalue buckling prediction done in Abaqus/Standard, and the buckling loads were calculated using the Riks solver in Abaqus/Standard. Based on the computed structural performance, evolutionary algorithms were used to update the design variables, then Rhino 3D reads the new variables and creates the next set of designs. The whole procedure was automated by our MATLAB script. [25] A standard genetic algorithm available in Matlab (GA-Matlab) [26] was used to obtain the results in Section IV, whereas in section V the Evolution Strategy with Covariance Matrix Adaption (CMA-ES) was adopted to study the effects of number of control points and symmetry. More details about CMA-ES can be found in [27, 28].

IV. Applications

In this section we present the designs of two imperfection-insensitive cylindrical shells. A design of an isotropic shell made from nickel is presented first and it is then compared with the Aster shell. Next, the design of a composite cylindrical shell is obtained. The optimization algorithm used in this section is GA-Matlab.

A. Isotropic Shells

The main objective of this design is to validate our approach by a comparison with the Aster shell. The radius, length, and thickness of the Aster shell are 75 mm, 120 mm and 153 μm , respectively. The Aster shell was subjected to axial compression, was clamped at both ends, and was made from nickel. In order to make a fair comparison with the Aster shell, the material properties, dimensions and boundary and loading conditions in our optimization were the same as those of the Aster shell. $N = 11$ control points were used to parameterize the cross-section and the maximum displacement allowed $w_{max} = 3$ mm. The optimization problem in this design is written as in Eq. 8.

1. Results

The genetic algorithm was run with 10 individuals in each generation and, the analysis was run for 100 generations. The results, shown in Fig. 12, give final buckling loads for perfect and imperfect shells of 21.29 KN and 20.25 KN, respectively, and the corresponding knockdown factor is 0.95. Note that the drop in critical buckling load, given by the difference between black and red curves, tends to decrease with the number of generations, hence the imperfection-sensitivity of the original shell has been greatly decreased. The final cross-sectional shape and the displacements of the control points are provided in Fig. 13.

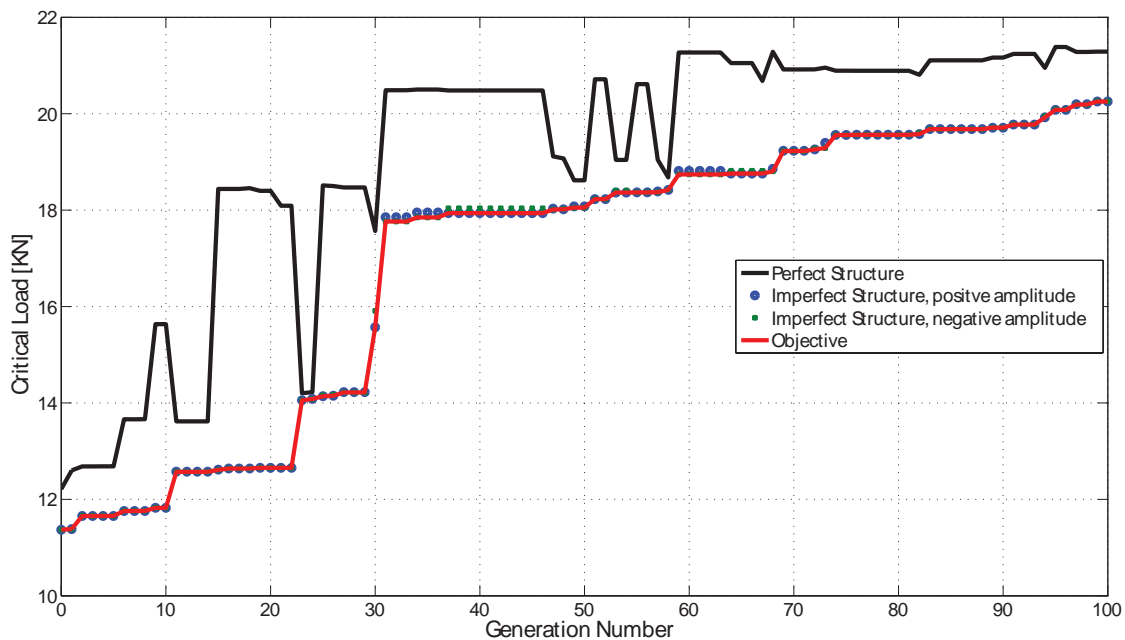


Figure 12: Evolution of objective function and buckling loads of perfect and imperfect structures, for isotropic cylindrical shell.

2. Comparison with Aster Shell

The simulated and measured buckling loads for the reference circular cylindrical shell, the Aster shell, and also our new design, are shown in Table 1. The buckling loads of the perfect shells obtained from the simulations are used as a reference to calculate the knockdown factors. Since these three structures have

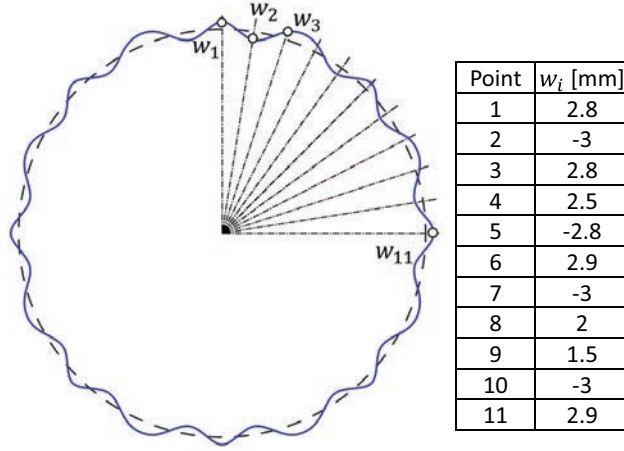


Figure 13: Optimized isotropic cylindrical wavy shell and corresponding displacements of control points.

different geometries and mass, the critical buckling stresses have been calculated in each case, to compare their performance.

We were not able to make or obtain nickel shells to test experimentally our wavy shell design. To compare with the Aster shell and the circular shell, the higher value between the buckling load of imperfect shells from simulations and the experimentally obtained value were used to define the critical buckling loads for the Aster shell and the circular shell. The critical stresses of the circular cylindrical shell (measurement), the Aster shell (simulation) and their knockdown factors are 56.8%, 80.7%, 80.7% and 93.7% of our wavy shell, respectively. This comparison indicates that the wavy shell obtained from our approach achieves not only higher buckling stress but also lower imperfection-sensitivity.

	Buckling Load [KN]			Knockdown Factor		Critical Stress [MPa]	
	Perfect	Imperfect	Test	Simulation	Test	Simulation	Test
Circular Shell	14.61	5.29	11.2	0.36	0.767	73.37	153.35
Aster Shell	18.33	16.40	14.4	0.89	0.786	217.9	187.44
Wavy Shell	21.29	20.25	N/A	0.95	N/A	270.12	N/A

Table 1: Knockdown factors, critical loads and stresses for isotropic cylindrical shell, Aster shell and circular shell.

B. Composite Cylindrical Shells

Composite cylindrical shells have been designed by the same methodology. The laminate in this design consists of six $30 \mu\text{m}$ thick laminae, $[+60^\circ, -60^\circ, 0^\circ]_s$, and is made from epoxy matrix and carbon fibers with fiber volume fraction of approximately 50%. The 0 direction of the laminate corresponds to the shell axial direction. The material properties of a lamina were measured experimentally: $E_1 = 127.9 \text{ GPa}$, $E_2 = 6.49 \text{ GPa}$, $G_{12} = 7.62 \text{ GPa}$, and $\nu_{12} = 0.354$, where E_1 is the longitudinal Young's modulus. The ABD matrix of the laminate was calculated from these properties, using classical lamination theory:

$$ABD = \begin{pmatrix} 9.919 \times 10^6 & 2.670 \times 10^6 & 0 & 0 & 0 & 0 \\ 2.670 \times 10^6 & 9.919 \times 10^6 & 0 & 0 & 0 & 0 \\ 0 & 0 & 3.625 \times 10^6 & 0 & 0 & 0 \\ 0 & 0 & 0 & 0.0108 & 0.0099 & 0.0034 \\ 0 & 0 & 0 & 0.0099 & 0.0373 & 0.0081 \\ 0 & 0 & 0 & 0.0034 & 0.0081 & 0.0125 \end{pmatrix} \quad (9)$$

where the units of the A and D matrices are N/m and Nm, respectively.

Considering the limitations of fabrication and testing, the dimensions of composite shell in optimization were chosen as follows:

$$\begin{aligned}
 \text{Thickness :} & \quad t = 180 \, \mu\text{m} \\
 \text{Radius :} & \quad R = 35 \, \text{mm} \\
 \text{Length :} & \quad L = 70 \, \text{mm} \\
 \text{Control points :} & \quad w_{max} = 1.5 \, \text{mm and } N = 11
 \end{aligned} \tag{10}$$

There were 10 individuals in each generation and the optimization was run for 50 generations. Fig. 14 shows the cross-section of the composite shell obtained in this way, as well as the corresponding displacements of the control points. The buckling loads of the perfect and imperfect wavy shells are 8.68 KN and 8.21 KN, respectively, and the knockdown factor is 0.95 which is 3.52 times larger than the circular composite shell. These results are summarized in Table 2. Although the wavy shell has a larger cross-sectional area, its critical stress, which excludes the effects of area of cross-section, is 6.58 times that of the circular shell.

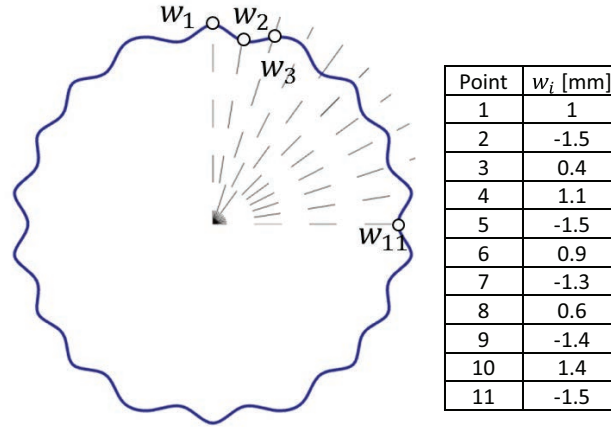


Figure 14: Composite cylindrical wavy shell and displacements of control points.

	Buckling Load [KN]		Knockdown Factor	Critical Stress [MPa]
	Perfect	Imperfect		
Circular Shell	4.15	1.14	0.27	28.8
Wavy Shell	8.68	8.21	0.95	189.54

Table 2: Critical loads, stresses and knockdown factors for optimized composite wavy cylindrical shell, as well as for circular shell. All data presented here are based only on simulations.

V. Relaxing Some Constraints

In previous sections, the cross-section was assumed to be symmetric with respect to the x and y -axes and only 11 control points in the first quadrant were employed to define the shape. In this section, these two geometric constraints are relaxed. Two cases with 11 and 16 controls points and mirror symmetry are studied in the first subsection. In the following subsection, designs of 4-fold symmetric shells with 10 and 15 control points are presented. We then conduct fourier analyses to get the spatial frequency components of each wavy cross-section. This section concludes with a comparison between these designs. All designs considered in this section are for composite shells with the $[+60^\circ, -60^\circ, 0^\circ]_s$ layup.

A. Effects of Number of Control Points

CMA-ES, a more efficient algorithm than GA-Matlab, was adopted in order to better search the design space. The symmetry and other geometric dimensions remain the same as in Eq. 10. The shell with 11

control points was also optimized using CMA-ES in order to make a fair comparison. The population size was 8 and the optimization was run for 150 generations. Figs. 15 and 16 show the evolution of the buckling loads of perfect and imperfect shells for these two designs.

For the wavy shell with 11 control points, $P_{imp,-}$ is almost always larger than P_{per} which is in turn larger than $P_{imp,+}$, suggesting that this analysis converges to a structure that behaves according to the Case I buckling discussed in Section II. The shell with 16 control points has almost equal buckling loads for both imperfect and perfect cases, therefore in this case the design has converged to the Case II buckling.

The knockdown factors are 0.921 and 0.994 for the wavy shells with 11 and 16 control points, respectively. The critical stresses, calculated from the lowest buckling load among the perfect shell and two imperfect shells, were 224.639 and 310.494 MPa, respectively, for 11 and 16 control points. The knockdown factor and critical stress of the shell with 16 control points are respectively 13.1% and 35.3% higher than the shell with 11 control points.

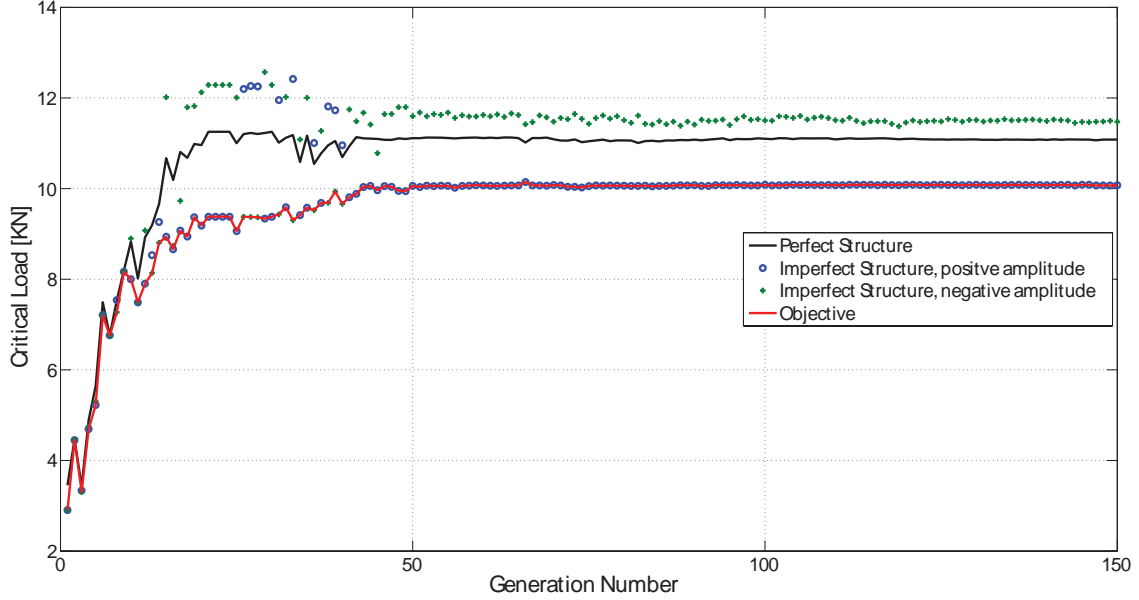


Figure 15: Evolution of buckling loads for mirror-symmetric wavy shell with 11 control points. The optimum occurs at the 66th generation, where the buckling loads for the perfect shell and the imperfect shells with positive and negative imperfections are 11.017, 10.145 and 11.420 kN, respectively.

The cross-sections of the two shells are shown in Fig. 17. We use a fourier analysis to compute the spatial frequency components of their cross-section, as shown in Fig. 18. The peak frequencies, which are defined as the frequencies with the maximum amplitudes, are respectively 17.58 and 21.48 m^{-1} for shells with 11 and 16 control points. The frequency components also show that the wavy shell with 16 control points has more high-frequency components. Defining the bandwidth of the spatial frequency as the maximum frequency whose amplitude is no less than 10% of the amplitude of the peak frequency, the bandwidths are calculated as 22.46 and 38.09 m^{-1} , respectively, for the wavy shells with 11 and 16 control points.

B. Effects of Symmetry

Wavy shells with 4-fold symmetry were also designed using the same optimization technique. Fig. 19 explains the definition of 4-fold symmetry. The first quarter of a shell has 10 or 15 control points which are equally spaced in the circumferential direction and the control points of the other three quarters are obtained by anticlockwise rotation of the first quarter for $\frac{\pi}{2}$, π and $\frac{3\pi}{2}$. In the first quarter, the angle of the i^{th} control point is:

$$\theta_{1,i} = \frac{2\pi}{N}(i-1), \quad i = 1, 2, 3, \dots, N \quad (11)$$

where N is the number of control points and here $N = 10, 15$. The angles of the control points in the q^{th} quarter were then derived from:

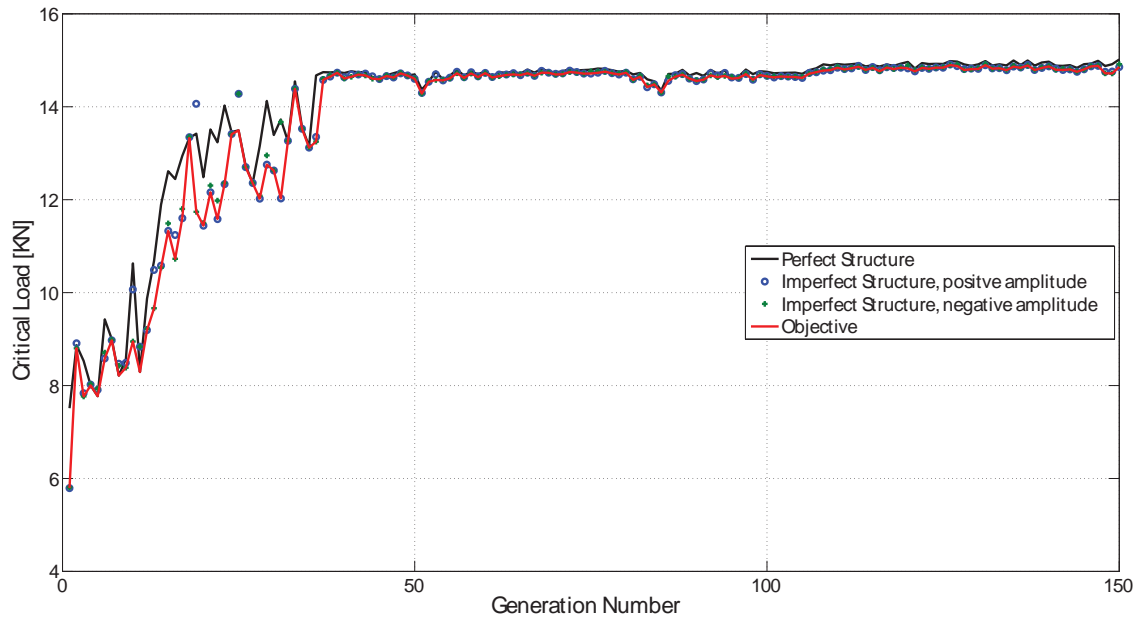


Figure 16: Evolution of buckling loads for mirror-symmetric wavy shell with 16 control points. The optimum occurs at the 126th generation, where the buckling loads for the perfect shell and the imperfect shells with positive and negative imperfections are 14.981, 14.908 and 14.897 KN, respectively.

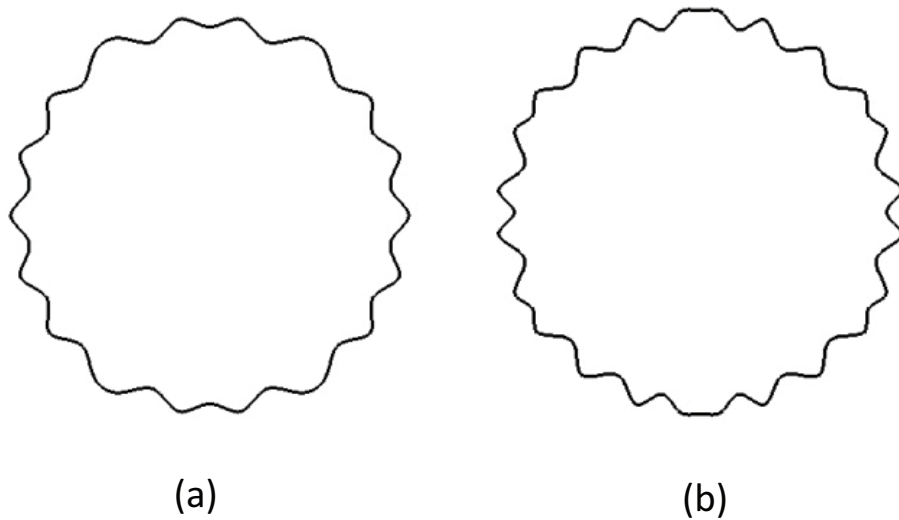


Figure 17: Shape of cross-section of mirror-symmetric wavy shells with (a) 11 and (b) 16 control points.

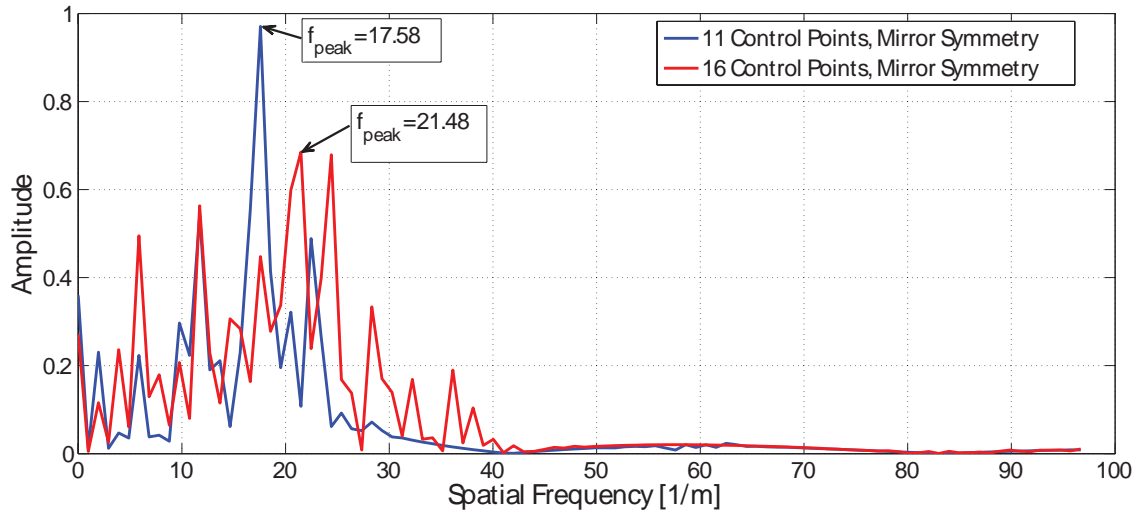


Figure 18: Spatial frequency of mirror-symmetric wavy shells.

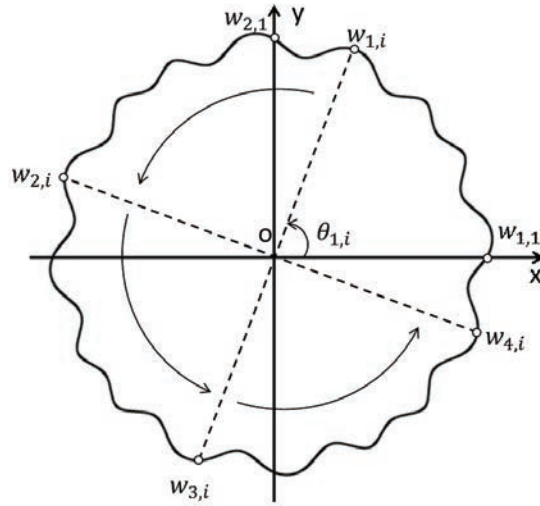


Figure 19: Schematic of 4-fold symmetry. $w_{q,i}$ and $\theta_{q,i}$ denote the displacement and angle of the i^{th} control point in the q^{th} quarter of a wavy shell.

$$\theta_{q,i} = \frac{2\pi}{N}(i-1) + (q-1)\frac{\pi}{2}, \quad q = 1, 2, 3, 4, \text{ and } i = 1, 2, 3, \dots, N \quad (12)$$

$\theta_{2,1}$ was calculated as $\pi/2$ by the above equations. This control point and the N control points of the first quarter divide the first quadrant into N sectors with equal angles. Although the number of control points in 4-fold symmetric shells is 1 less than the mirror-symmetric shells, they provide the same resolution as the mirror-symmetric shells.

The evolution of the buckling loads for both 4-fold symmetric shells is plotted in Figs. 20 and 21; both wavy shells converge to the Case II buckling. The knockdown factors were 0.879 and 0.994 for shells with 10 and 15 control points, respectively and the critical stresses were 208.224 and 281.712 MPa. These results show that increasing the number of control points leads to decreased imperfection-sensitivity and improved critical stresses.

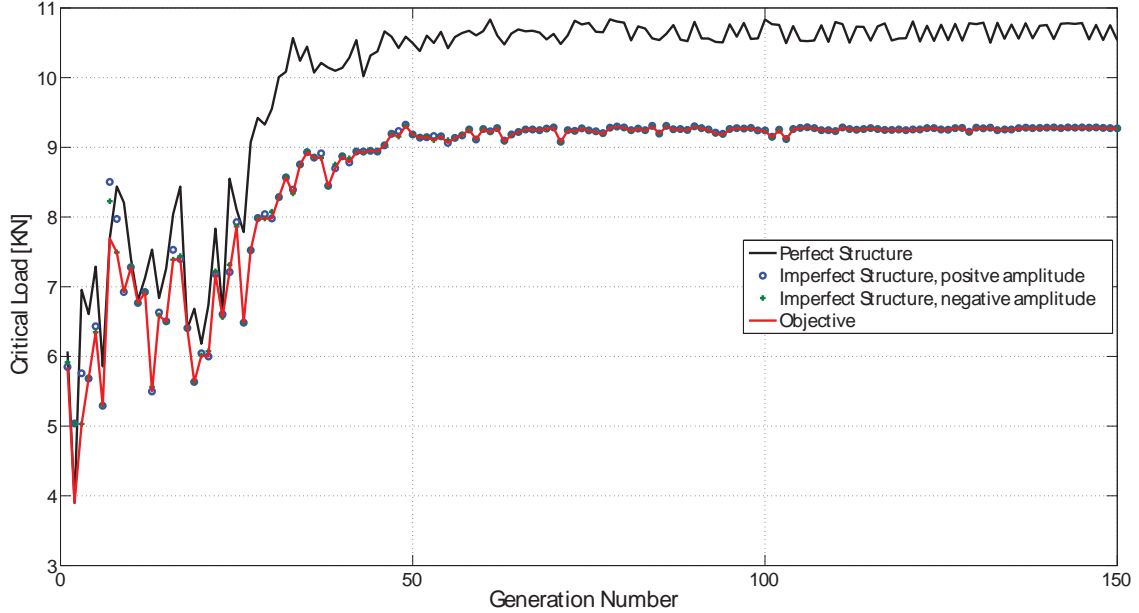


Figure 20: Evolution of buckling loads for 4-fold symmetric wavy shell with 10 control points. The best result is obtained at the 49th generation, where the buckling loads for perfect shell, imperfect shells with positive and negative imperfections are 10.587, 9.325 and 9.310 KN, respectively.

Fig. 22 shows the cross-sections of the two 4-fold symmetric shells obtained from this study. We also conducted a fourier analysis to obtain the spatial frequency components of the 4-fold symmetric shells, see Fig. 23. The peak frequencies for 4-fold symmetric wavy shells with 10 and 15 control points were 11.72 and 19.53 m^{-1} , and the bandwidths 24.41 and 36.13 m^{-1} , respectively.

C. Comparison

The results obtained in this section are summarized in Table 3. Compared with mirror-symmetric wavy shells, the corresponding 4-fold symmetric wavy shells have lower critical stresses and smaller or equal knockdown factors, suggesting that the assumption of mirror symmetry provides better performance than 4-fold symmetry. The results also indicate that higher peak spatial frequencies and wider bandwidths tend to lead to higher critical stresses.

VI. Experiments

This section presents the results obtained from buckling tests carried out on the composite wavy shell whose cross-section had been obtained by means of the genetic algorithm, in Section IV (Fig. 14), and also on composite circular cylindrical shells. The fabrication technique is presented first, followed by the method

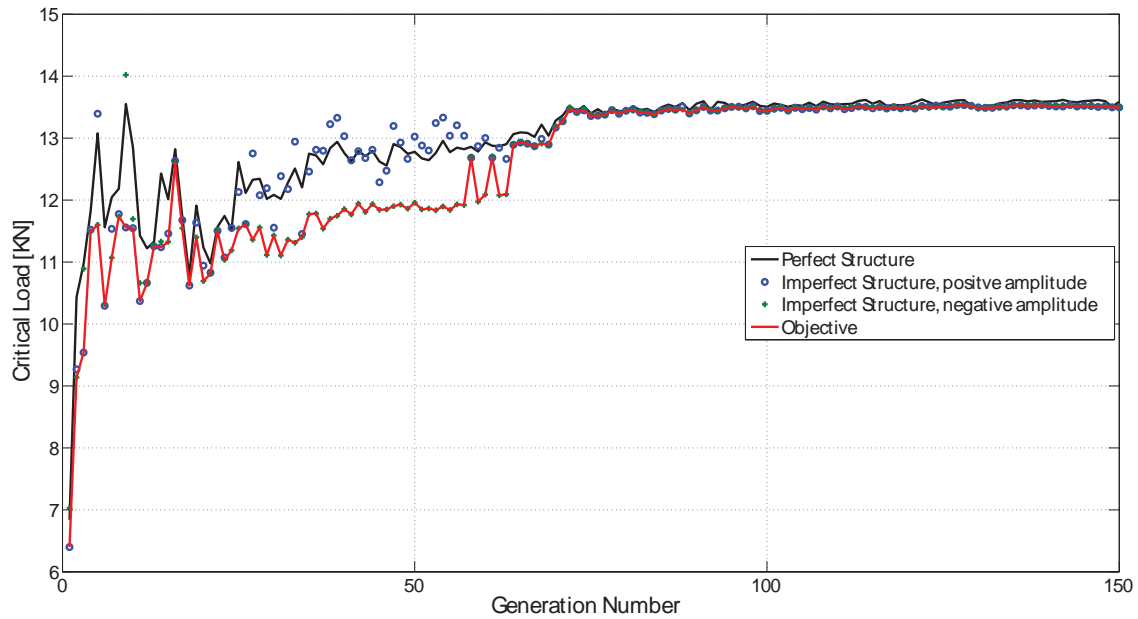


Figure 21: Evolution of buckling loads for 4-fold symmetric wavy shell with 15 control points. The best result is obtained at the 127th generation, where the buckling loads for perfect shell, imperfect shells with positive and negative imperfections are 13.609, 13.535 and 13.536 kN, respectively.

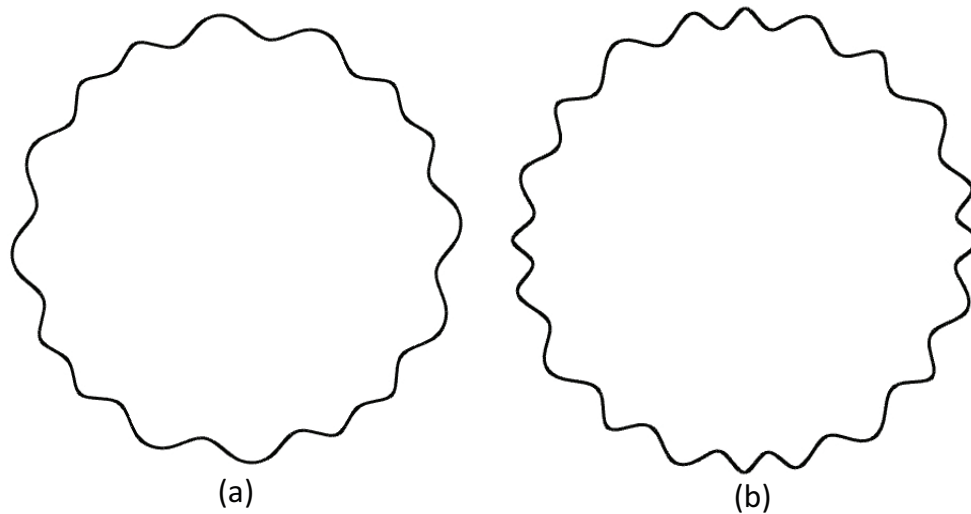


Figure 22: Shape of cross-section of 4-fold symmetric wavy shells with (a) 10 and (b) 15 control points.

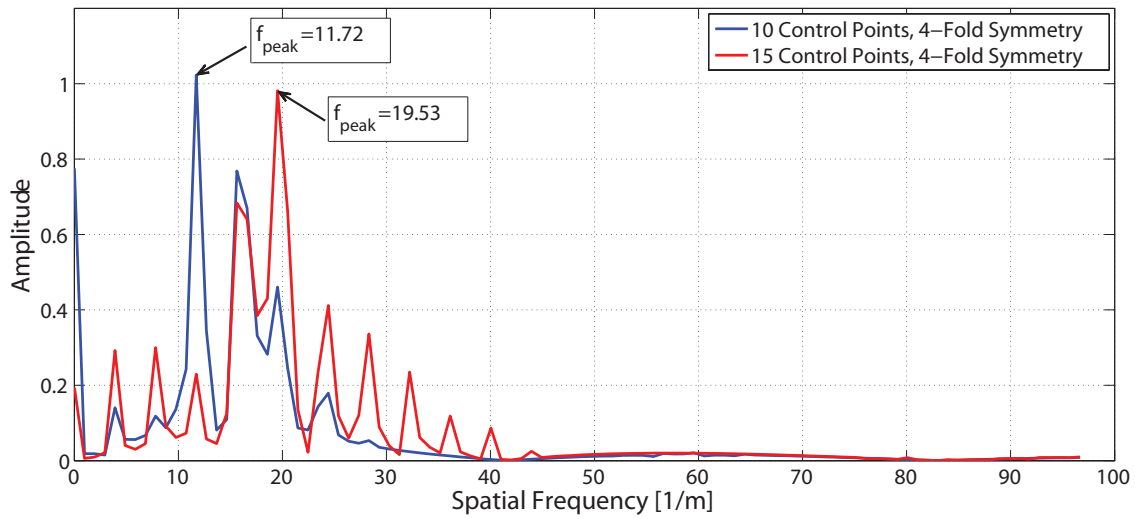


Figure 23: Spatial frequency of 4-fold symmetric wavy shells.

Symmetry	Control Points	Buckling Load [KN]		Knockdown Factor	Critical Stress [MPa]	Peak Frequency	Bandwidth
		Perfect	Imperfect				
Mirror	11	11.017	10.145	0.921	224.639	17.58	22.46
	16	14.981	14.897	0.994	310.494	21.48	38.09
4-Fold	10	10.587	9.310	0.879	208.244	11.72	24.41
	15	13.609	13.536	0.994	281.712	19.53	36.13

Table 3: Summary of results for mirror-symmetric and 4-fold symmetric composite wavy shells.

to measure imperfections and by the experimental setup. The test results are presented at the end of the section.

A. Fabrication

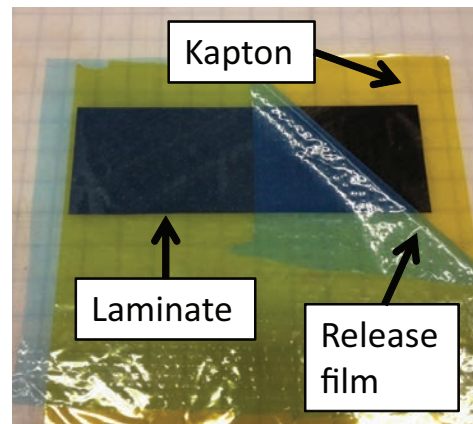
The shells were made from unidirectional prepreps of ThinPregTM120EPHTg manufactured by North Thin Ply Technology LLC. Our current fabrication approach makes use of a male steel mandrel made on a wire-cut EDM machine, shown in Fig. 24 (a). The cross-section shown in Fig. 14 represents the shell's mid-plane, so the male mandrel is half shell thickness smaller than the middle plane cross-section. To prevent separation of the laminate from the male mandrel during lay-up and curing, a female mold cut into four parts was made. The female mold pushes the laminate onto the male mandrel during curing. To facilitate the separation of the shell from the mandrel after curing, we added a 25-micron thick Kapton film between the male mandrel and the laminate, as seen in Fig. 24 (b). The Kapton film remains bonded to the shell, however it is thin and much softer than the composite material. Calculations show that the change of buckling loads due to the Kapton is around 1%, therefore its influence is ignored. The blue film in Fig. 24 (b) is a perforated release film that helps release excessive epoxy during curing.

The laminate and two film layers were first squeezed onto the mandrel, then the pieces of the female mold were slid onto the mandrel one by one, from one end to keep the shape, see Fig. 25 (a-b). The mandrel, Kapton film, laminate, release film and female mold were then covered with a breather blanket, Fig. 25 (c). The mandrels, laminate and all wrapping materials were put in a vacuum bag and then cured in an autoclave.

The recommended curing procedure, plotted in Fig. 26, was applied. The temperature of the autoclave was ramped up to 80°C at a rate of 2°C/min and held at 80°C for 10 minutes to let the resin flow and fully impregnate the laminate. The temperature was then ramped up to 120°C at 2°C/min and then held constant for 2 hours. The laminate was then cooled down to room temperature at 2°C/min. The laminate was held

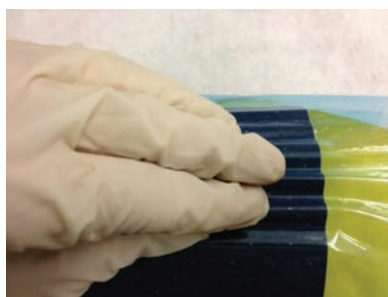


(a)

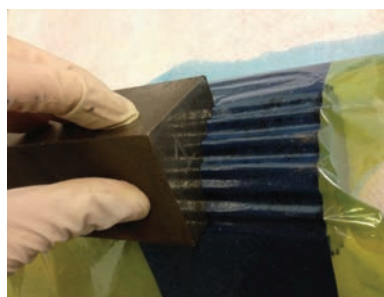


(b)

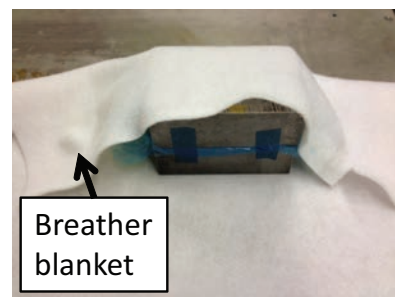
Figure 24: (a) Male mandrel and female mold; (b) laminate and films that facilitate release of cured shell.



(a)



(b)



(c)

Figure 25: Lay-up.

under vacuum through the entire process. All the wrapping materials and female mold were removed after cooling down. Before releasing the shell from the male mandrel, both ends were polished using sand paper.

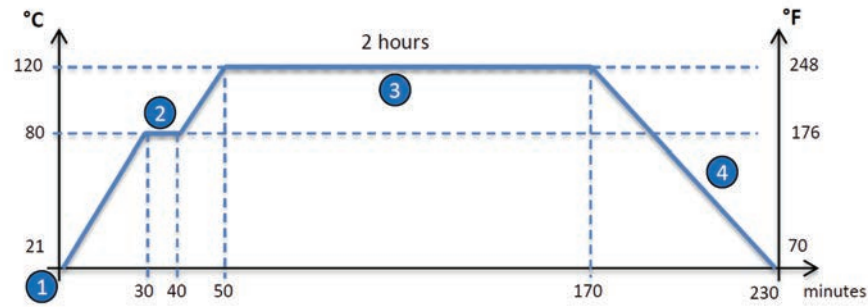


Figure 26: Curing cycle for ThinPreg™120EPHTg, courtesy of North Thin Ply Technology.

Clamped boundary conditions were obtained by potting the shells into room temperature cure epoxy. The epoxy was poured into a plastic shell with open ends held on a piece of glass, as shown in Fig. 27 (a). Tapes were used to fix the plastic shell on the glass and to prevent leakage of the epoxy. The glass was covered by a layer of Frekote release agent to facilitate the removal of the cured epoxy. The thin cylindrical shell requires extreme care to avoid large deformation when potting the shell into epoxy. The female mold was mounted on two flat aluminum blocks of the same thickness, as seen in Fig. 27 (b). The shell was held in the female mold and slid down into the epoxy. This setup avoids any deformation of the shell due to transverse forces and also ensures that the cylindrical shell is perpendicular to the glass. Shells with cured epoxy on one end are much stiffer and hence potting on the second end was done without using the female mandrel. A hole was drilled on the cured epoxy base to let the air flow out from the shell when potting on the second end. The amount of epoxy poured into the plastic shell was carefully controlled to achieve the desired shell length. Measurements show that the error in shell length was less than 3% for all potted shells.

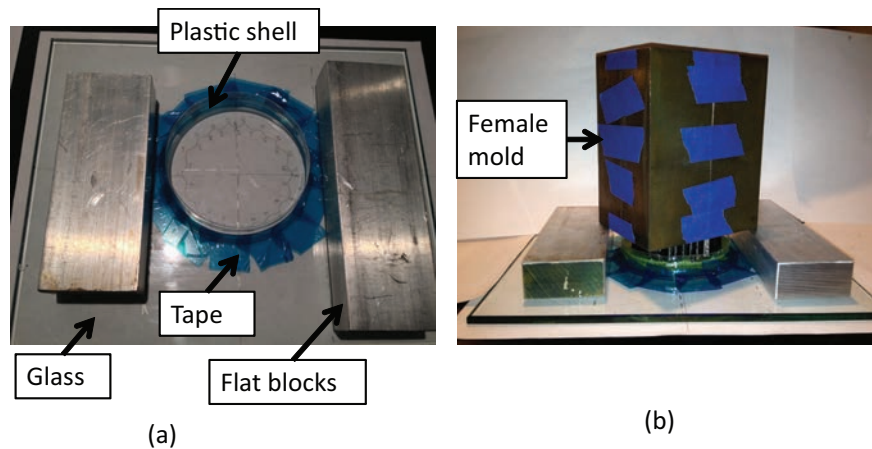


Figure 27: Setup for potting.

B. Measurement of Geometry

A photogrammetry technique was chosen to measure the shape of the shells. The commercial photogrammetry software Photomodeler 5 [29] was used with two types of targets. Coded targets are black circular spots surrounded by black segments of rings, as seen in Fig. 28 (a). The shape of these rings is non-repetitive such that each coded target can be uniquely detected by the software. In our measurement the coded targets are attached to the top and lateral surfaces of the cured epoxy base. Non-coded targets are regular black dots projected onto the shell surface by means of an LCD projector. The shells had been painted white to facilitate the detection of the non-coded targets.

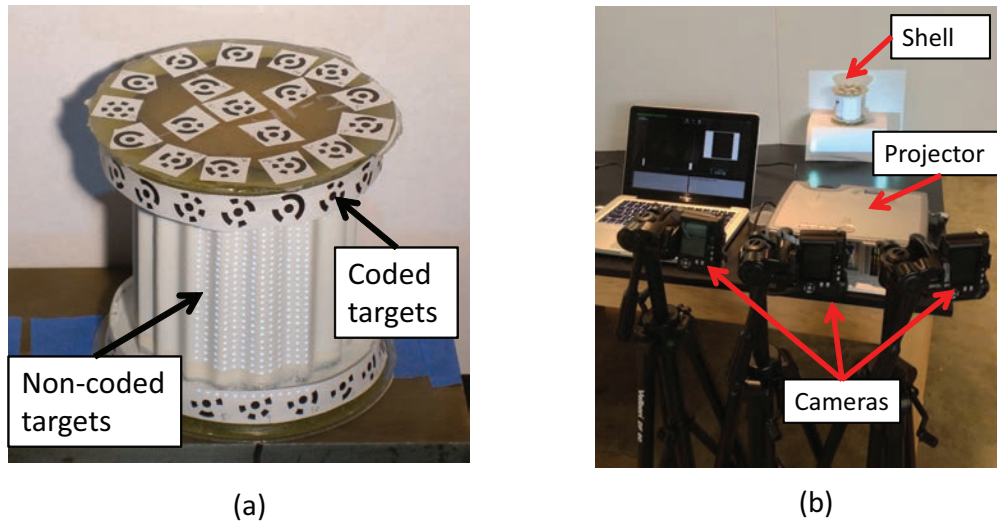


Figure 28: (a) Coded and non-coded targets. (b) Setup for shape measurements.

The setup for measuring the shell geometry is shown in Fig. 28 (b). There are three steps involved in a measurement. In the first step the coded targets are photographed and correlated to define a global coordinate system. Only the center camera was used in this step, and it is higher than the shell so as to record the targets on the top surface of the epoxy base. The shells were rotated between 18 and 23 times such that all coded targets can be photographed by the camera. The photos were processed with Photomodeler 5. All photos included the coded targets on the top surface of the epoxy base, to act as fiducials in the final correlation of all data. Three non-collinear coded targets on the top surface were picked to define the O,X, Y plane, and the distance between two of these points provides a scale for the measurement.

The second step obtains the positions of the non-coded targets projected on the shell surface. We used three cameras pointed in different directions to photograph the shell surface. The second camera was at the same height as the other two. Photomodeler was used to correlate the coded and non-coded targets in these three photos with the photos taken in the first step to calculate their coordinates in the global coordinate system. Ideally, the surface of the measured object should be perpendicular to the projection direction in order to project perfect circular targets on the object. Highly distorted targets may not be correctly correlated. In our measurements we projected the non-coded targets only onto a narrow rectangular area, as seen in Fig. 28, where its surface is roughly perpendicular to the projection direction. Hence, we had to rotate the shell multiple times to obtain the complete geometry. The coordinates of the non-coded targets obtained from a measurement were exported to a text file for post-processing.

The third step is to combine the points obtained in the previous step to obtain the complete shape. Rhino 3D was employed to read the text files containing the coordinates of the targets and to combine these points into a single geometry. The coordinates of all measured points are based on the coordinate system defined by three arbitrarily selected coded targets on the top surface of the epoxy base. However, in order to calculate imperfections, the measured coordinates need to be referenced to a coordinate system coaxial with the theoretically defined shell surface. A three-parameter transformation was defined in terms of translations in the x and y directions and rotation with respect to the z -axis, and the square of the distance between measured and designed shapes was computed. The coordinate transformation was determined by minimizing the square distance with CMA-ES. For easier convergence we first manually moved the measured cluster of points to a position close to the designed shape, Fig. 29 (a), and then started the iteration.

The optimization can be expressed as follows:

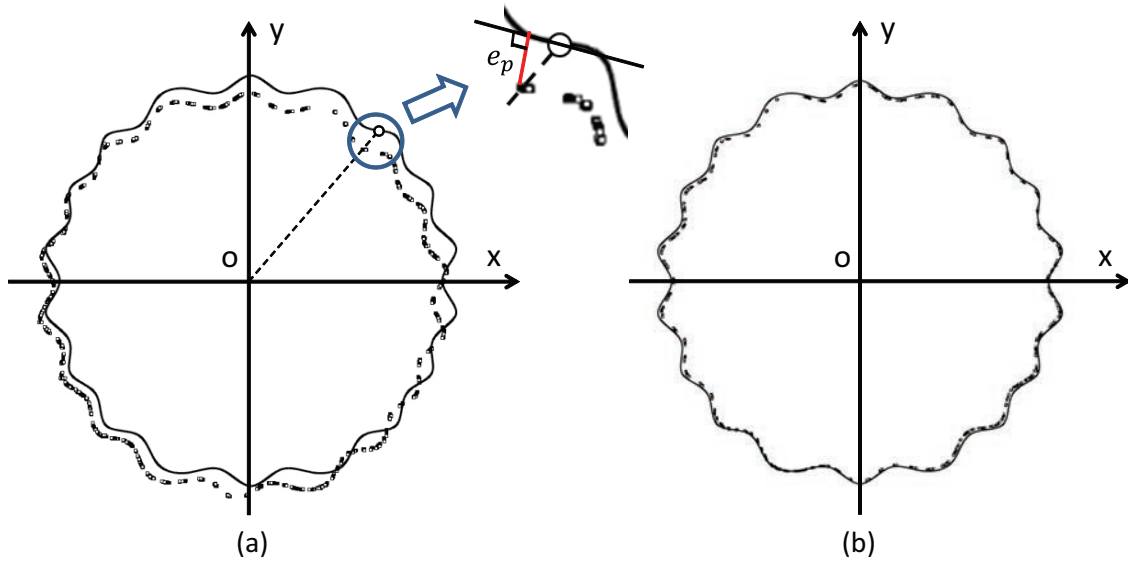


Figure 29: Schematic of finding the coaxial position of measured and theoretically-defined shell shells. In (a) e_p is the normal distance between the p^{th} measured point and the corresponding point on the perfect shell; (b) coaxial position of measured points found by minimizing the square distance.

$$\begin{aligned}
 &\text{Minimize : } \sum_{p=1}^M e_p^2 \\
 &\text{Subject to : } (1) \quad |T_x| \leq 10 \text{ mm} \\
 &\quad \quad \quad (2) \quad |T_y| \leq 10 \text{ mm} \\
 &\quad \quad \quad (3) \quad |R_z| \leq \frac{\pi}{2}
 \end{aligned} \tag{13}$$

where e_p , T_x , T_y and R_z are the normal distance, translations in the x and y directions, and rotation with respect to the z -axis, respectively. M denotes the total number of measured points.

This process provides the coaxially defined shape measurements shown in Fig. 29 (b). Three wavy shells and one circular shell were measured. The imperfections of circular shell 1 and wavy shell 1 are presented in Figs. 30 and 31. These figures show that the imperfections are more uniform in the axial direction than in the circumferential direction. Plots of the imperfections of the other wavy shells are provided in the Appendix.

The thickness distribution of the shells were measured before potting the ends. We measured thickness at the heights of 0 cm, 2 cm, 3.5 cm, 5 cm and 7 cm on each hill, valley, as well as the middle points between the hill and valley of each corrugation. Figs. 32 and 33 show the thickness distributions of wavy shell 1 and circular shell 1. The thickness distributions of the other wavy shells are provided in the Appendix.

The mean and standard deviation for the thickness and imperfection amplitude for each shell are listed in Table 4. The standard deviations of the thickness of circular shell 1 and wavy shells 1 and 2 are 6.64%, 10.55% and 13.95% of the shell thickness, respectively. However, wavy shell 3 has a significantly larger standard deviation of 19.51%. The thickness distributions of the wavy shells (Figs. 32, 42 and 43) show that their thickness is as thin as around 130 μm . The imperfection amplitudes are 4.23, 6.10, 5.46 and 6.87 times the corresponding shell thickness, respectively, for circular shell 1 and wavy shells 1, 2 and 3.

C. Testing and Results

Four mirror-symmetric wavy shells obtained in Section III and two circular shells were tested. Fig. 34 shows the setup for the buckling tests, using an Instron testing machine and the Vic3D digital image correlation (DIC) system to record the shell deformation during the test.

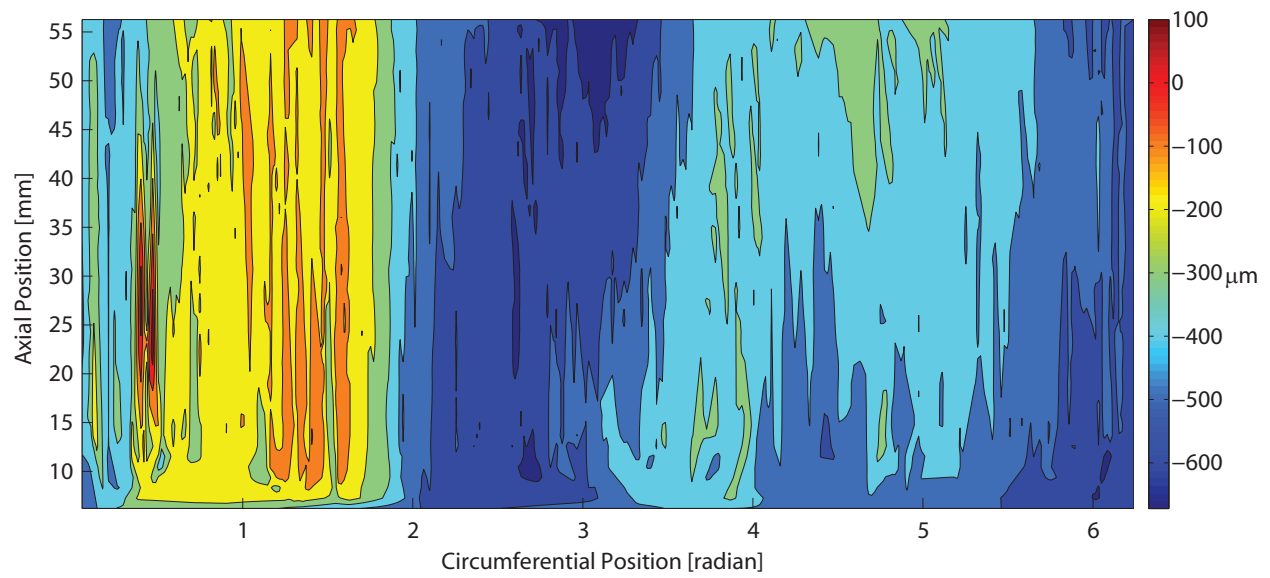


Figure 30: Imperfection distribution of circular shell 1.

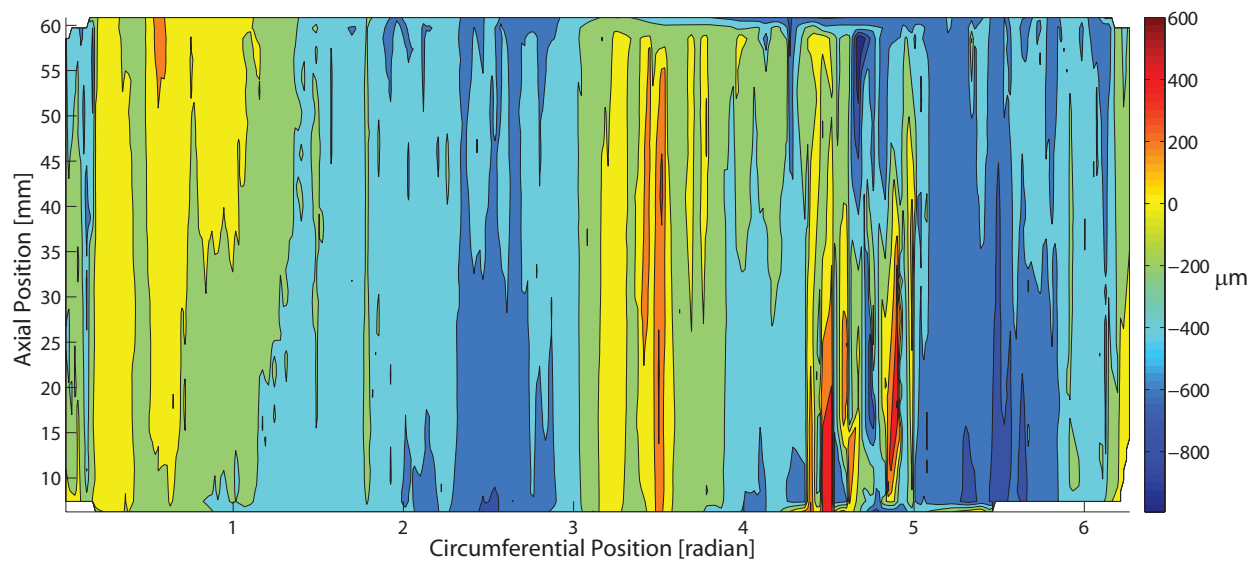


Figure 31: Imperfection distribution of wavy shell 1.

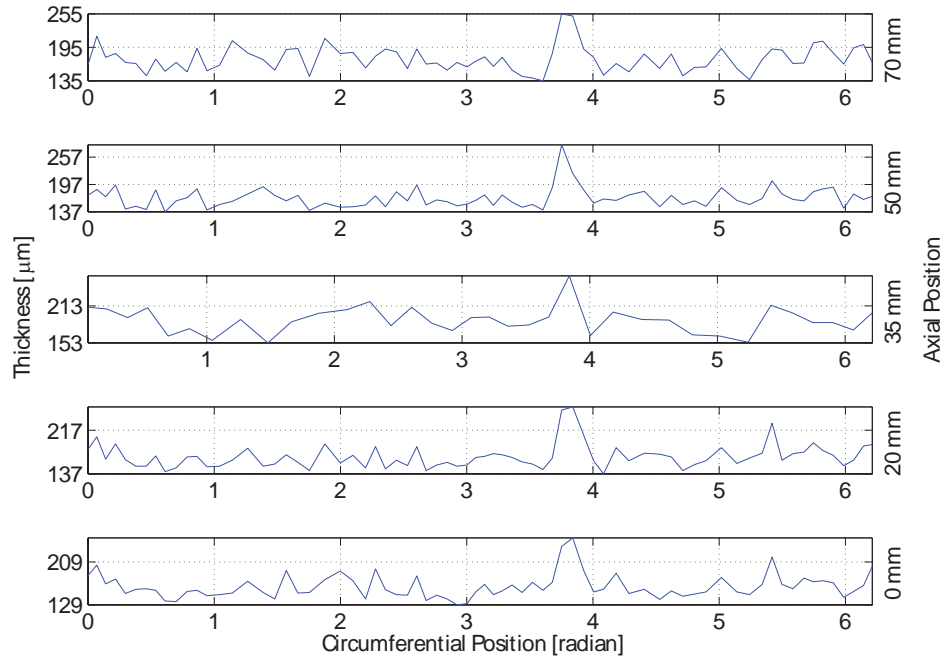


Figure 32: Thickness distribution of wavy shell 1.

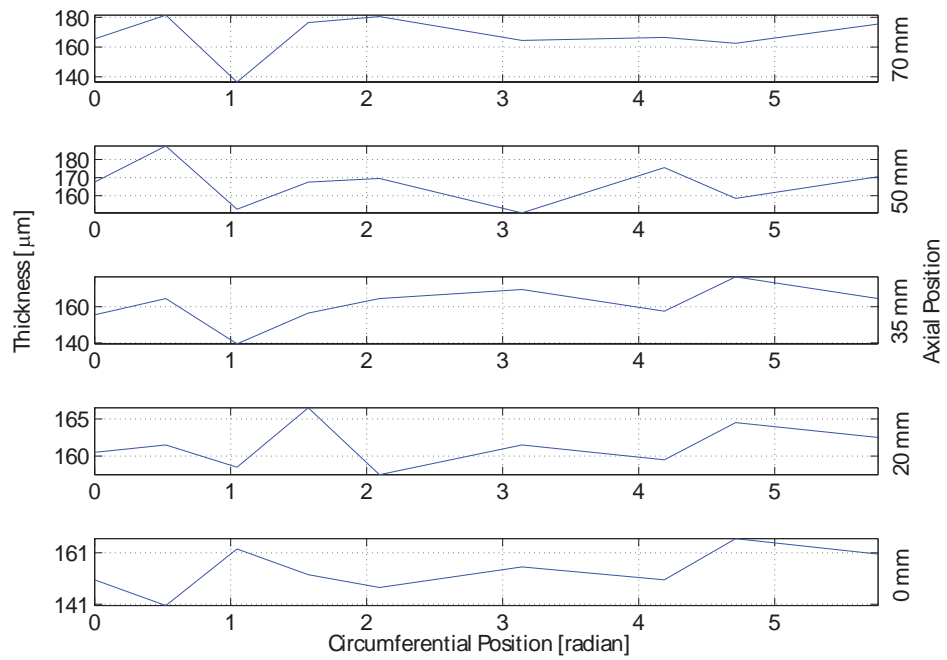


Figure 33: Thickness distribution of circular shell 1.

Shells	Thickness [μm]	Amplitude of Imperfections [μm]	μ
Circular shell 1	162 \pm 11	685	4.23
Circular shell 2	N/A	N/A	N/A
Wavy shell 1	171 \pm 24	1043	6.10
Wavy shell 2	170 \pm 18	928	5.46
Wavy shell 3	170 \pm 33	1168	6.87
Wavy shell 4	N/A	N/A	N/A

Table 4: Measured thickness and imperfections of circular and wavy shells. The thickness and imperfection amplitude of circular shell 2 and wavy shell 4 were not measured.

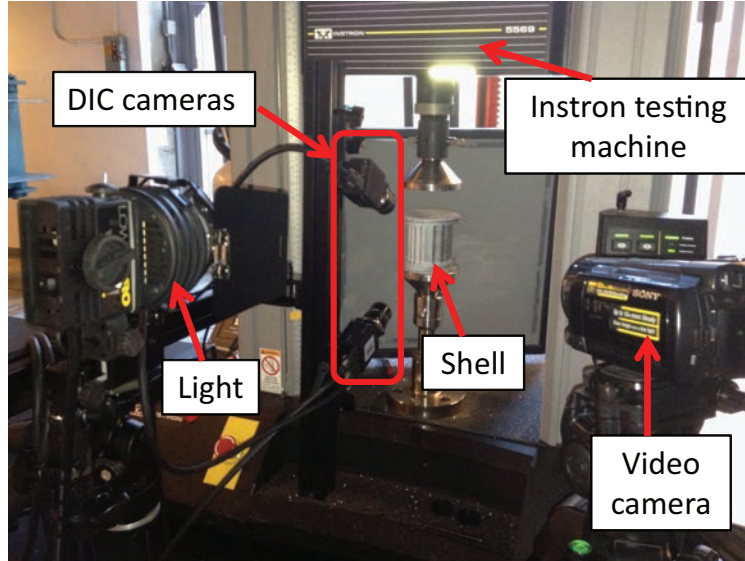


Figure 34: Experimental setup for buckling tests.

The buckling loads are summarized in Table 5. The knockdown factors of the circular shells are 0.48 and 0.32, respectively, confirming that circular shells are very sensitive to imperfections. The knockdown factors of wavy shells 2 and 4 are 0.995 and 0.972, respectively. Although the knockdown factors of wavy shells 1 and 3 are lower than our predictions, they are still respectively 68.5% and 64.2% higher than circular shell 1. The experimental results are discussed in the next section.

	Buckling Load [KN]			Knockdown Factor		Critical Stress [MPa]	
	Perfect	Imperfect	Test	Simulation	Test	Simulation	Test
Circular Shell 1	4.15	1.14	2.00	0.27	0.48	28.80	47.96
Circular Shell 2			1.32		0.32		33.35
Wavy Shell 1	8.68	8.21	7.02	0.95	0.809	189.54	171.19
Wavy Shell 2			8.64		0.995		211.30
Wavy Shell 3			6.84		0.788		167.21
Wavy Shell 4			8.44		0.972		194.85

Table 5: Knockdown factors, critical loads and stresses for optimized composite wavy shells obtained in Section III and circular shells.

Typical shapes of the shells after buckling are shown in Fig. 35. The circular cylindrical shell buckles into a diamond shape, and is able to recover its shape after unloading. The buckled shape of the wavy shell

is localized in a nearly circumferential crease and there is a significant amount of damage along the crease.

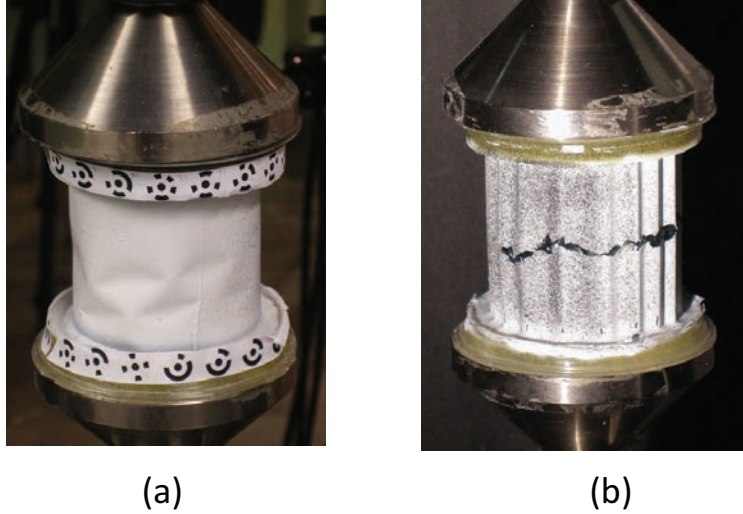


Figure 35: Buckling modes of (a) circular shell 1 and (b) wavy shell 1.

VII. Discussion

A. Sensitivity to Shape Imperfections

Recall that during the optimization the shape of the critical imperfection was assumed to coincide with the critical buckling mode and its amplitude was assumed to be equal to the shell thickness. The imperfection distribution of the wavy shell obtained in Section IV (B) has been plotted in Fig. 36. Note that the measured imperfections, shown in Figs 31, 40 and 41, do not resemble the critical buckling mode.

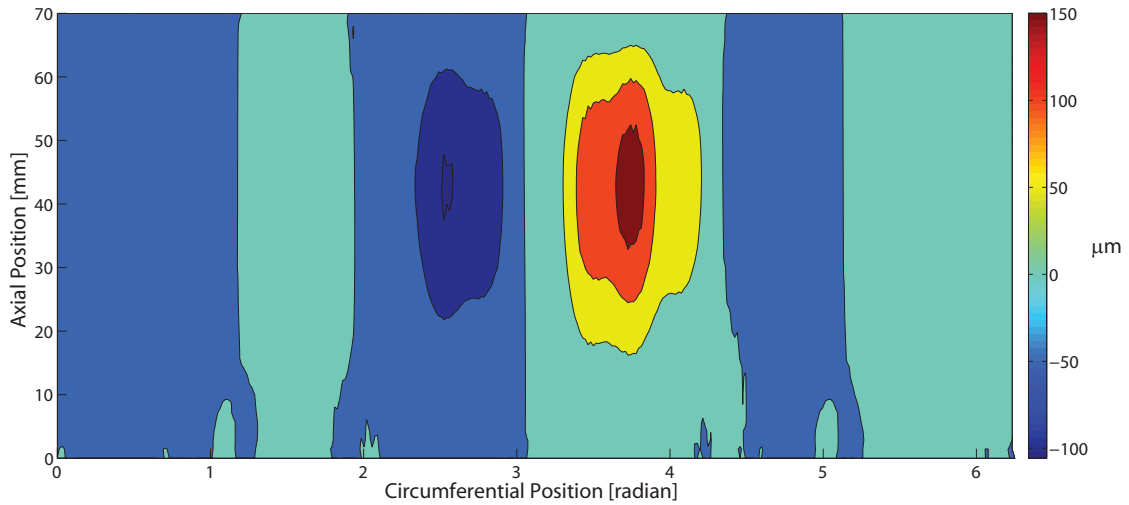


Figure 36: Calculated imperfection distribution of wavy shell obtained in Section IV (B).

The maximum measured amplitude of all imperfections is $6.87t$, which is much larger than the shell thickness used in the optimization study. Hence, before comparing our predictions with the experimental data, we have calculated the buckling loads using the same imperfection distribution as before, shown in Fig. 36, and amplitudes up to $8t$. The results in Fig. 37 (a) show that the knockdown factor decreases to 35.8% when the imperfection amplitude is equal to 8 times the shell thickness. Considering these latest results, all measured knockdown factors are larger than the predicted values, once the correct imperfection

amplitudes are used, and hence the predictions provide lower bounds on the experimental buckling loads.

We have also calculated the knockdown factors of all other composite wavy shells with imperfection amplitudes of up to $8t$, the results are shown in Fig. 37 (b). The knockdown factor of the mirror-symmetric wavy shell with 16 control points decreases by only 7.14%, from 0.994 to 0.923, when the imperfection amplitude increases to $8t$. Fig. 37 (b) also shows that the 4-fold symmetric shell with 10 control points has lower imperfection-sensitivity than mirror-symmetric shells with 11 control points when the amplitudes of imperfections are large. Both simulations and experiments have shown that the optimized wavy shells have successfully avoided the extreme imperfection-sensitivity of cylindrical shells.

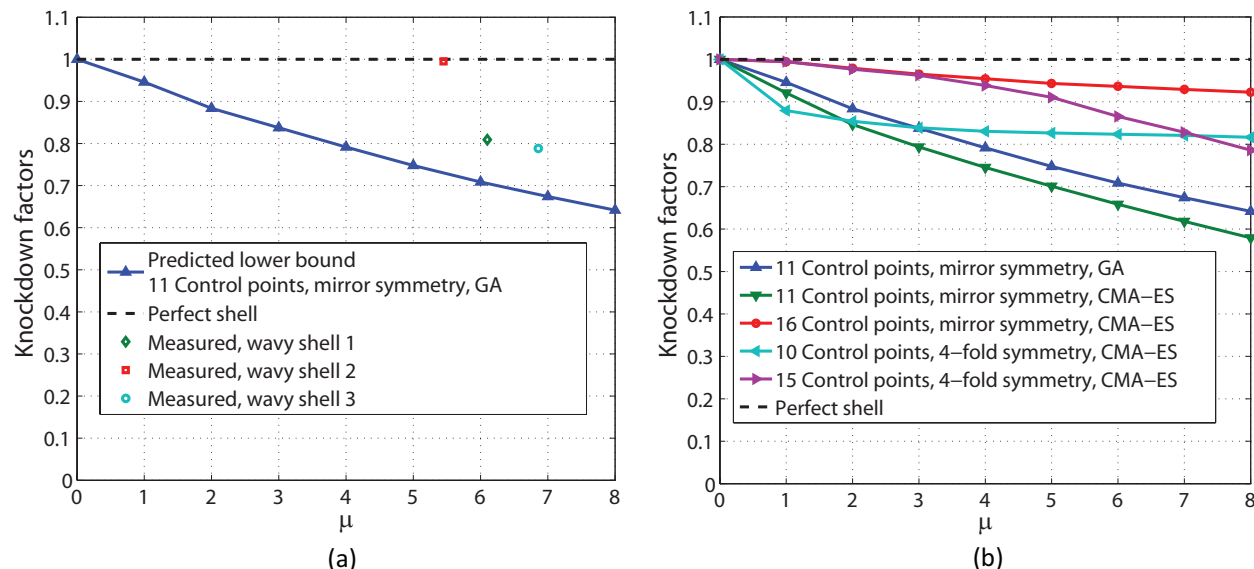


Figure 37: (a) Predicted lower bound on knockdown factors of composite wavy shell obtained by GA in Section IV (B). (b) Predicted lower bounds on knockdown factors of all optimized composite wavy shells.

B. Influence of Non-uniformity of Shell Thickness

In our optimization we assumed that the shell thickness is uniform. However, the data presented in Table 4 shows that the thickness has standard deviations up to 20%. The precritical and postbuckling strain fields have been analyzed to study the influence of shell thickness. The initiation of buckling in wavy shell 1 was captured by the DIC system, and the axial strains ε_x are plotted in Fig. 38. Since buckling starts in areas of high compressive axial strain, several possible initial buckling positions have been identified in Fig. 38 (a). Fig. 38 (b) suggests that buckling started in area 2. The shell thickness is another factor influencing the buckling initiation position. The average thicknesses of areas 1, 2 and 3 are 175, 164 and 180 μm , respectively. It is likely that the smaller thickness in area 2 leads to the initial buckling occurring here. The precritical and postbuckling strain fields for wavy shells 2 and 3 are plotted in Figs. 44 and 45 in the Appendix. The initial buckling positions of wavy shells 2 and 3 were not recorded by the DIC system. However, both the creases on their buckled surface go through the potential critical position where the shells have large compressive strain and small thickness.

The experimentally obtained knockdown factors of wavy shells and their thickness, as well as the thickness at (potential) critical positions, are presented in Table 6. The larger knockdown factor corresponds to larger shell thickness at potential critical position and smaller variation of averaged shell thickness. Hence, the non-uniformity of the shell thickness is also a significant factor influencing the knockdown factor.

C. Efficiency of Wavy Shells

Inspired by the concept of the *shape factor* introduced by Ashby [30] in order to compare beams with different cross-sectional shapes, we introduce the efficiency factor of a general cylindrical shell subject to axial compression, to quantify its efficiency. Recall that the relation between weight and load indices for

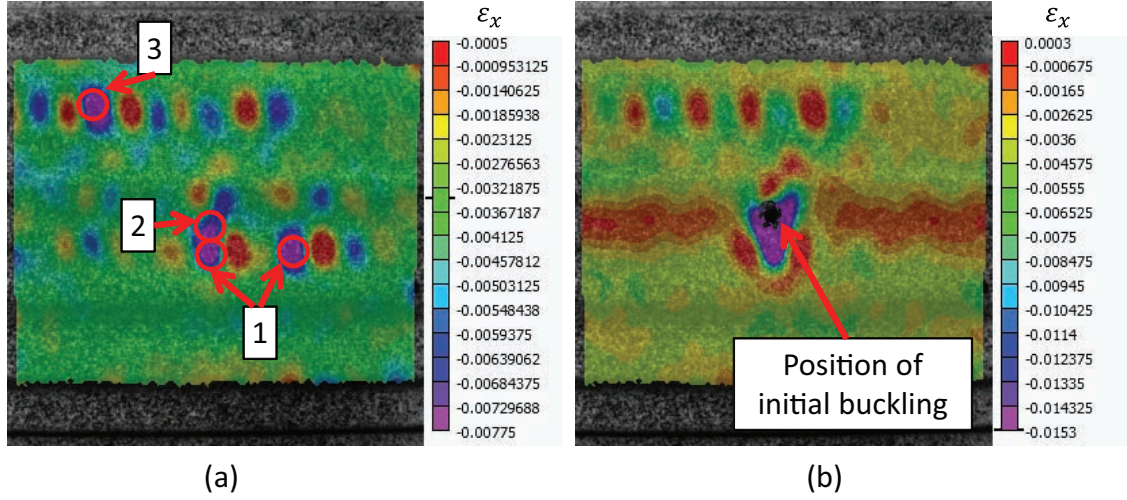


Figure 38: (a) Precritical axial strain field. The possible initial buckling positions are shown by circles 1, 2 and 3. (b) Position where buckling started. The shell axis is horizontal in these pictures.

Shells	Average Thickness [μm]	Thickness at (Potential) Critical Position [μm]	Knockdown factor
Wavy shell 1	171 ± 24	164	0.809
Wavy shell 2	170 ± 18	186	0.995
Wavy shell 3	170 ± 33	164	0.788
Wavy shell 4	N/A	N/A	0.972

Table 6: Summary of shell thickness.

perfect circular cylindrical shells has the expression, Eq. 7:

$$\frac{W}{AR} = \rho \left(\frac{\sqrt{3(1-\nu^2)}}{\gamma E} \right)^{\frac{1}{2}} \left(\frac{N_x}{R} \right)^{\frac{1}{2}} = \left(\frac{\gamma E}{\rho^2 \sqrt{3(1-\nu^2)}} \right)^{-\frac{1}{2}} \left(\frac{N_x}{R} \right)^{\frac{1}{2}} \quad (14)$$

We define the efficiency factor, ξ , for arbitrary cylindrical shells such that:

$$\frac{W}{AR} = \left(\frac{N_x}{R} \right)^{\frac{1}{2}} \xi^{-\frac{1}{2}} \quad (15)$$

and hence for circular cylindrical shells

$$\xi = \frac{\gamma E}{\rho^2 \sqrt{3(1-\nu^2)}} \quad (16)$$

Larger ξ correspond to shells with higher Young's modulus and lower density. Eq. 14 also suggests that larger ξ results in a higher load index for the same weight index. Hence, we can use ξ as a quantity to describe the efficiency of shells under axial compression.

Eq. 15 plots as a straight line with slope of 0.5 in the log-log plot of weight and load indices. Shells of equal efficiency lie on the same line, which is therefore called *iso-efficiency line*. We have added the experimentally obtained buckling loads of the wavy shells listed in Table 5 as well as the predicted buckling load of the mirror-symmetric wavy shell with 16 control points in the performance chart in Fig. 39. The blue line corresponds to perfect ($\gamma = 1$) aluminum circular shells.

Using Eq. 15, the efficiency of wavy shell 2 and the mirror-symmetric wavy shell with 16 control points can be calculated as $2.21\xi_a$ and $3.07\xi_a$, respectively, where ξ_a is the efficiency of perfect aluminum circular cylindrical shells. Thus, the efficiency of these wavy shells is 121% and 207% higher than the perfect

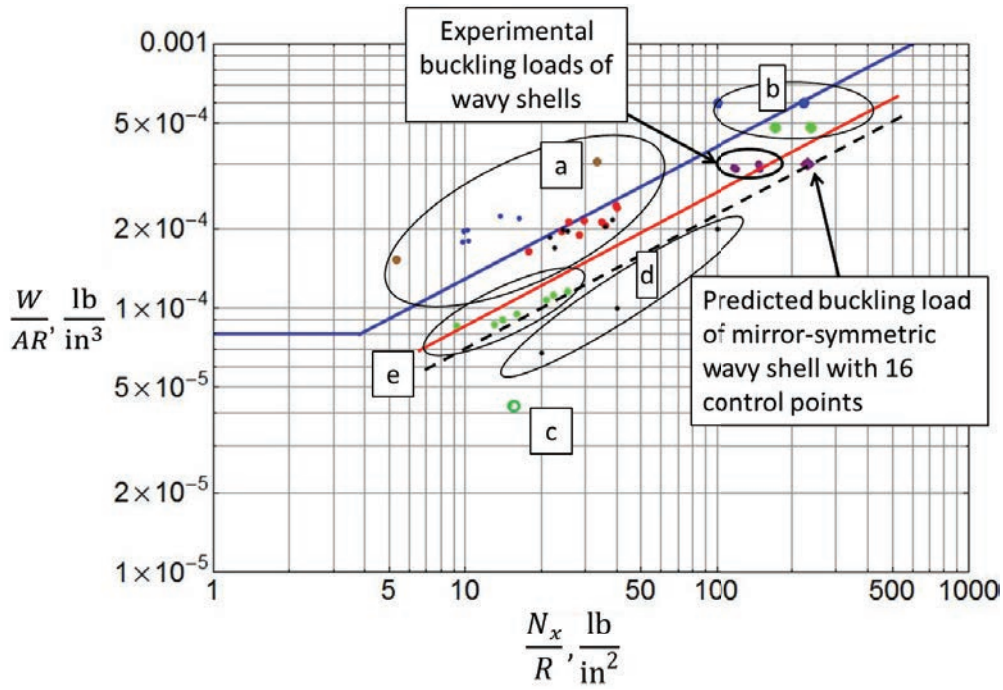


Figure 39: Performance of stiffened shells with experimental data of composite wavy shells obtained in section IV and predicted data of mirror-symmetric shell of 16 control points. Iso-efficiency lines for our wavy shells are plotted as the red solid line and black dash line, respectively.

aluminum circular cylindrical shells. The iso-efficiency line of wavy shell 2 in Fig. 39 indicates that it has higher efficiency than the stiffened shells in groups a and b. The predicted iso-efficiency line of the mirror-symmetric wavy shells with 16 control points shows that its efficiency is higher than groups a, b and e.

VIII. Conclusion

The objective of this study was to adopt shape optimization techniques to obtain imperfection-insensitive cylindrical shells. Ramm's method to reduce imperfection-sensitivity has been successfully incorporated in the design of imperfection-insensitive shells. We introduced the concept of a wavy shell whose cross-section is obtained by NURBS interpolation of radially defined control points. Wavy shells made of isotropic and composite materials have been designed in this study. The optimized isotropic wavy shell has a knockdown factor of 0.95. In comparison with the experimental results of Aster shell, the simulated knockdown factor, buckling load and critical stress are increased by 20.9%, 40.6% and 44.1%, respectively. Composite wavy shells have been designed using the same technique. The simulated knockdown factor, buckling load and critical stress of the obtained composite wavy shells are respectively 251.9%, 620.2% and 558.1% higher than the circular composite cylindrical shell.

We also studied the effects of the number of control points and the type of symmetry assumed in the analysis. The results show that increasing the number of control points tends to increase both critical stress and knockdown factor. Wavy shells with mirror symmetry and 4-fold symmetry have been designed and compared. The comparison shows that mirror-symmetric wavy shells have better performance than those with 4-fold symmetry. We also conducted fourier analyses to obtain the spatial frequency components of wavy shells. The spatial frequency analysis shows that wavy shells with better performance have both higher peak frequency and wider bandwidth. The efficiency of the optimized wavy shells has been quantified by introducing efficiency factors and iso-efficiency lines. Comparisons based on tested wavy shells show that the efficiency is 121% higher than the perfect aluminum circular cylindrical shell.

We constructed four composite wavy shells and validated our approach by means of experiments. Large variations in thickness and large amplitudes of imperfections were observed. Composite wavy shells 2 and

4 have knockdown factors of 0.995 and 0.972, respectively, indicating that we have obtained practically imperfection-insensitive behavior. Composite wavy shells 1 and 3 have knockdown factors of 0.809 and 0.788, respectively, which are still beyond our predictions for the corresponding amplitude of imperfections, however it was found that these shells had particularly large deviations in shape and thickness distribution.

Acknowledgements

We thank Dr. Martin Mikulas (National Institute of Aerospace) and Professor Ekkehard Ramm (University of Stuttgart) for helpful comments and advice, and Professor Petros Koumoutsakos (ETH Zurich) for recommending the CMA-ES algorithm to us. We also thank John Steeves (Caltech) for providing the properties of the composite material used in the present study, Keith Patterson and Ignacio Maqueda (Caltech) for help and advice regarding the fabrication and testing of wavy shells. Financial support from the Resnick Institute at California Institute of Technology is gratefully acknowledged.

References

- ¹Brush, D. O. and Almroth, B. O., "Buckling of Bars, Plates, and Shells", New York, McGraw-Hill, 1975, pp. 225-262.
- ²Jones, R. M., "Buckling of Bars, Plates, and Shells", Blacksburg, Virginia, Bull Ridge Corporation, 2006, pp. 654-689.
- ³Singer, J., Arbocz, J. and Weller, T., "Buckling Experiments: Experimental Methods in Buckling of Thin-Walled Structures: Vol. 2." New York, Wiley, 2002.
- ⁴Ramm, E. and Wall, W. A., "Shell Structures – a Sensitive Interrelation between Physics and Numerics", *International Journal for Numerical Methods in Engineering*, Vol. 60, issue 1, pp. 381-427, 2004.
- ⁵Reitinger, R., Bletzinger, K. U. and Ramm, E., "Shape Optimization of Buckling Sensitive Structures", *Computing Systems in Engineering*, Vol. 5, pp. 65-75, 1994.
- ⁶Reitinger, R. and Ramm, E., "Buckling and Imperfection Sensitivity in the Optimization of Shell Structures", *Thin-walled structures*, Vol. 23, pp. 159-177, 1995.
- ⁷Thompson, J. M. T., "Optimization as a Generator of Structural Instability", *International Journal of Mechanical Sciences*, Vol. 14, pp. 627-629, 1972.
- ⁸Hutchinson, J. W. and Koiter, W. T., "Postbuckling Theory", *Applied Mechanics Reviews*, Vol. 23, issue 12, pp. 1353-1366, 1970.
- ⁹Elishakoff, I., "Probabilistic Resolution of the Twentieth Century Conundrum in Elastic Stability", *Thin-walled structures*, Vol. 59, pp. 35-57, 2012.
- ¹⁰von Karman, T. and Tsien, H. S., "The Buckling of Thin Cylindrical Shells under Axial Compression", *Journal of the Aeronautical Sciences*, Vol. 8, pp. 303-312, 1941.
- ¹¹Donnell, L. H. and Wan, C. C., "Effects of Imperfections on Buckling of Thin Cylinders and Columns under Axial Compression", *Journal of Applied Mechanics*, Vol. 17, pp. 73-83, 1950.
- ¹²Koiter, W. T., "The Effect of Axisymmetric Imperfections on the Buckling of Cylindrical Shells under Axial Compression", *Proc. K. Ned. Akad. Wet.*, Amsterdam, ser. B, vol. 6, 1963; also, *Lockheed Missiles and Space Co. Rep. 6-90-63-86*, Palo Alto, Calif., 1963.
- ¹³Koiter, W. T., "On the Stability of Elastic Equilibrium", thesis(in Dutch with English summary), Delft, H. J. Paris, Amsterdam, 1945. English translation, *Air Force Flight Dym. Lab. Tech. Rep.*, AFFDL-TR-70-25, 1970.
- ¹⁴Peterson, J. P., Seide, P. and Weingarten, V. I., "Buckling of Thin-Walled Circular Cylinders", NASA SP-8007, 1965.
- ¹⁵Nemeth, M. P. and Starnes, J. H., "The NASA Monographs on Shell Stability Design Recommendations: a Review and Suggested Improvements", NASA TP-1998-206290, 1998.
- ¹⁶Hilburger, M. W. and Starnes, J. H., "High-Fidelity Nonlinear Analysis of Compression-Loaded Composite Shells", AIAA Paper 2001-1394, 2001.
- ¹⁷Hilburger, M. W., Nemeth, M. P. and Starnes, J. H., "Shell buckling Design Criteria Based on Manufacturing Imperfection Signatures", *AIAA Journal*, Vol. 44, issue 3, pp. 654-663, 2006.
- ¹⁸Card, M. F. and Jones, R. M., "Experimental and Theoretical Results for Buckling of Eccentrically Stiffened Cylinders", NASA TN D-3639, 1966.
- ¹⁹Peterson, J. P., "Structural Efficiency of Ring-Stiffened Corrugated Cylinders in Axial Compression", NASA TN D 4073, August 1967.
- ²⁰Agarwal, B. L. and Sobel, L. H., "Weight Optimized Stiffened, Unstiffened, and Sandwich Cylindrical Shells", *J. Aircraft*, Vol 14, NO, 10, 1977.
- ²¹Nemeth, M. and Mikulas, M. M., "Simple Formulas and Results for Buckling-Resistance and Stiffness Design of Compression-Loaded Laminated-Composite Cylinders", NASA TP-2009-215778, 2009.
- ²²Scott, N. D., Harding, J. E. and Dowling, P. J., "Fabrication of Small Scale Stiffened Cylindrical Shells", *Journal of Strain Analysis*, Vol. 22, pp. 97-106, 1987.
- ²³Jullien, J. F. and Araar, M., "Towards an Optimal Cylindrical Shell Structures under External Pressure", *Buckling of shell structures, on land, in the sea, and in the air*, Elsevier Applied Science, London, pp. 21-32, 1991.
- ²⁴Hughes, T. J. R., Cottrell, J. A. and Bazilevs, Y., "Isogeometric Analysis: CAD, Finite Elements, NURBS, Exact Geometry and Mesh Refinement", New York, Wiley, 2009.

- ²⁵Ning, X. and Pellegrino, S., “Design of Lightweight Structural Components for Direct Digital Manufacturing”. 53rd AIAA/ASME/ASCE/AHS/ASC Structures, Structural Dynamics and Materials Conference, 23-26 April 2012 Honolulu, Hawaii.
- ²⁶A. J. Chipperfield and P. J. Fleming, “The MATLAB Genetic Algorithm Toolbox”, Department of Automatic Control and Systems Engineering of The University of Sheffield, UK.
- ²⁷Hansen, N., Müller, S. D. and Koumoutsakos, P., “Reducing the Time Complexity of the Derandomized Evolution Strategy with Covariance Matrix Adaptation (CMA-ES)”, *Evolutionary Computation*, Vol. 11, pp. 1-18, 2003.
- ²⁸Hansen, N., “The CMA Evolution Strategy: A Tutorial”, 2011.
- ²⁹EosSystems, “PhotoModeler Pro 5, User Manual”, 2004.
- ³⁰Ashby, M., “Material Selection in Mechanical Design”, Oxford, Butterworth-Heinemann, 2005.

Appendix

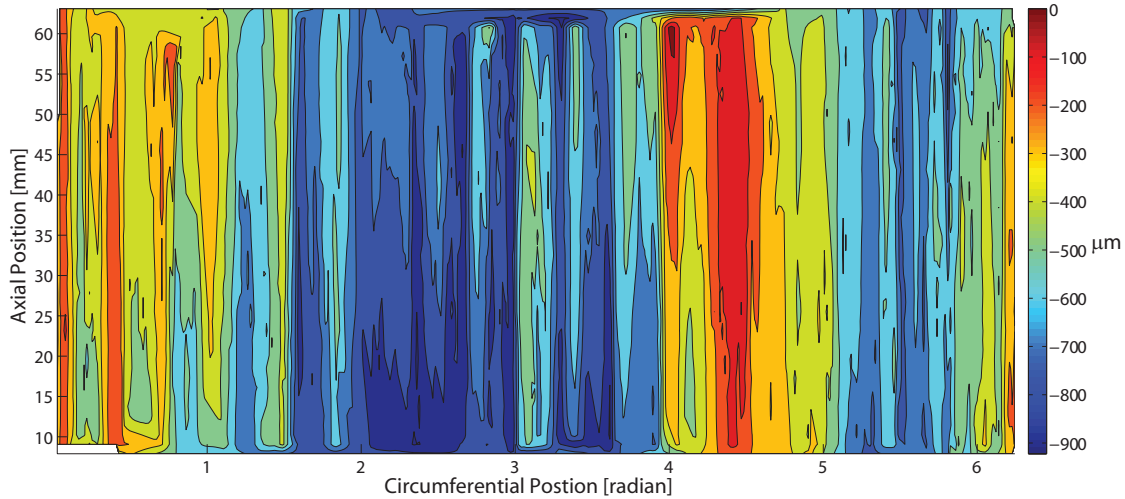


Figure 40: Imperfections of wavy shell 2.

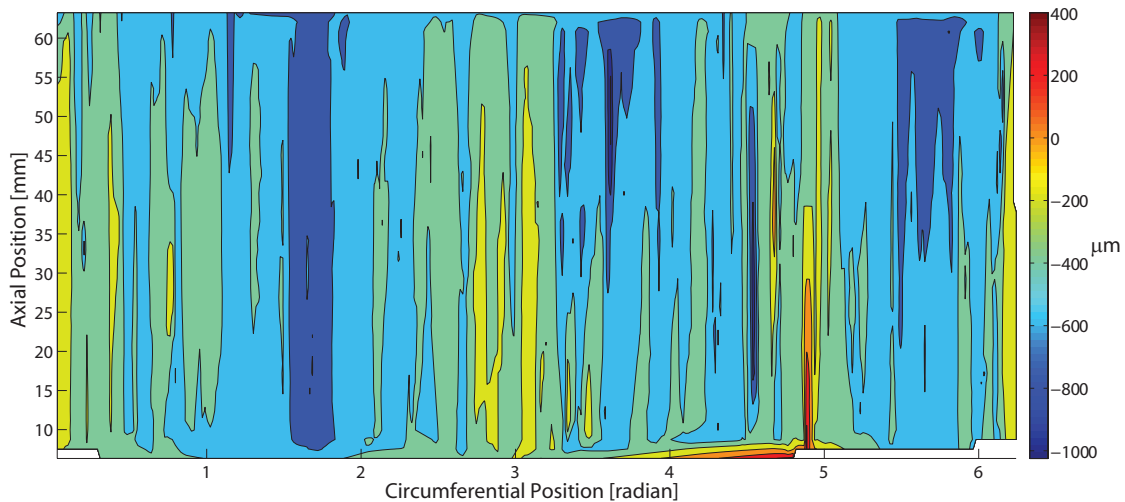


Figure 41: Imperfections of wavy shell 3.

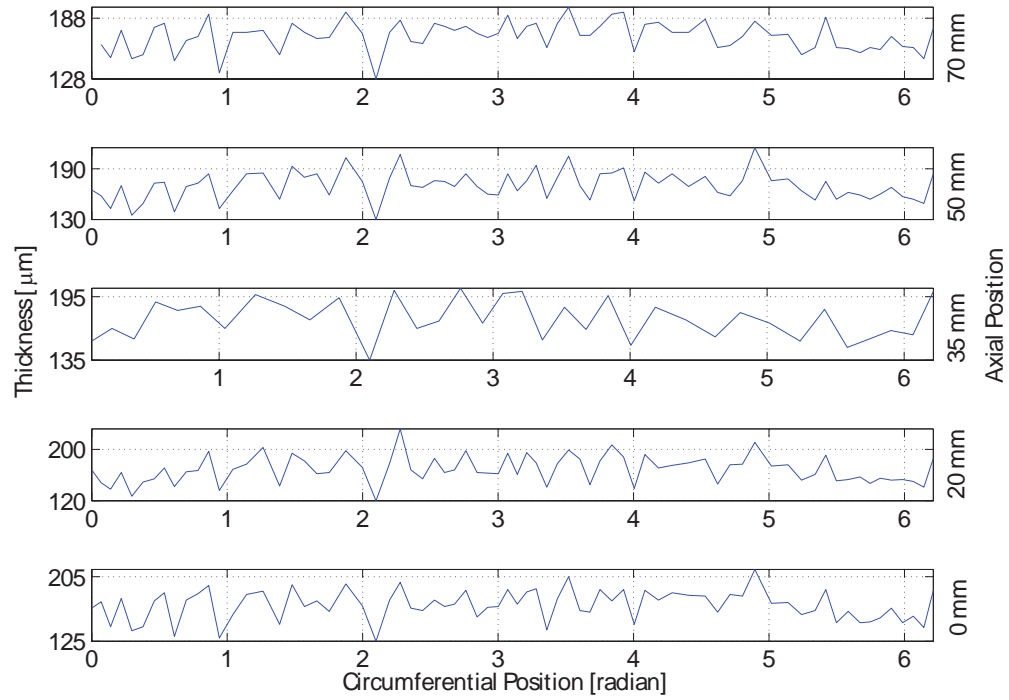


Figure 42: Thickness distribution of wavy shell 2.

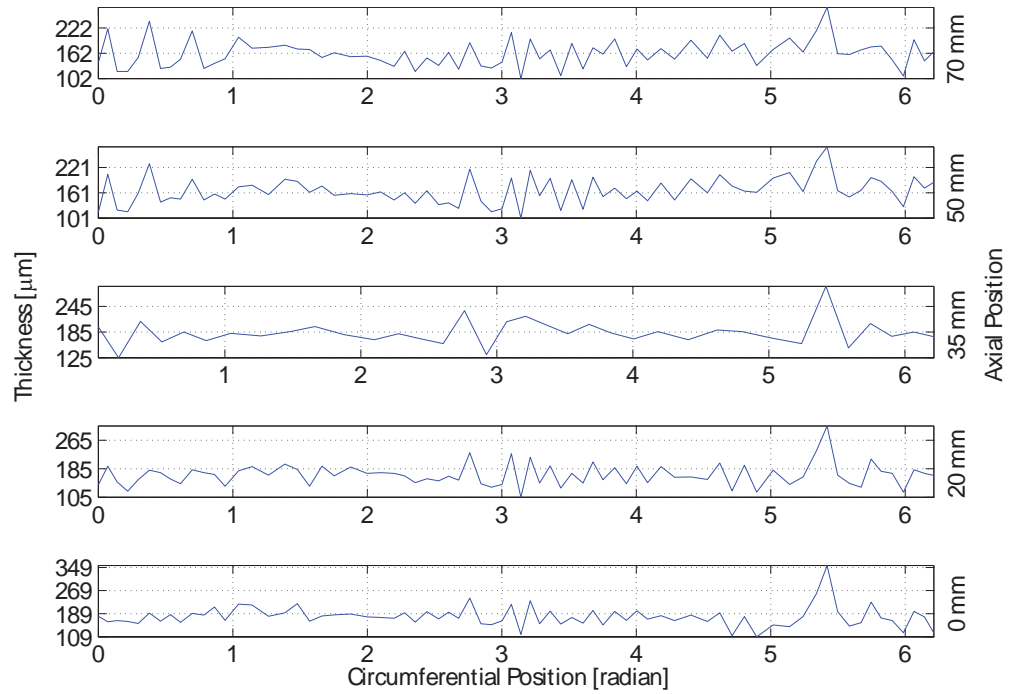


Figure 43: Thickness distribution of wavy shell 3.

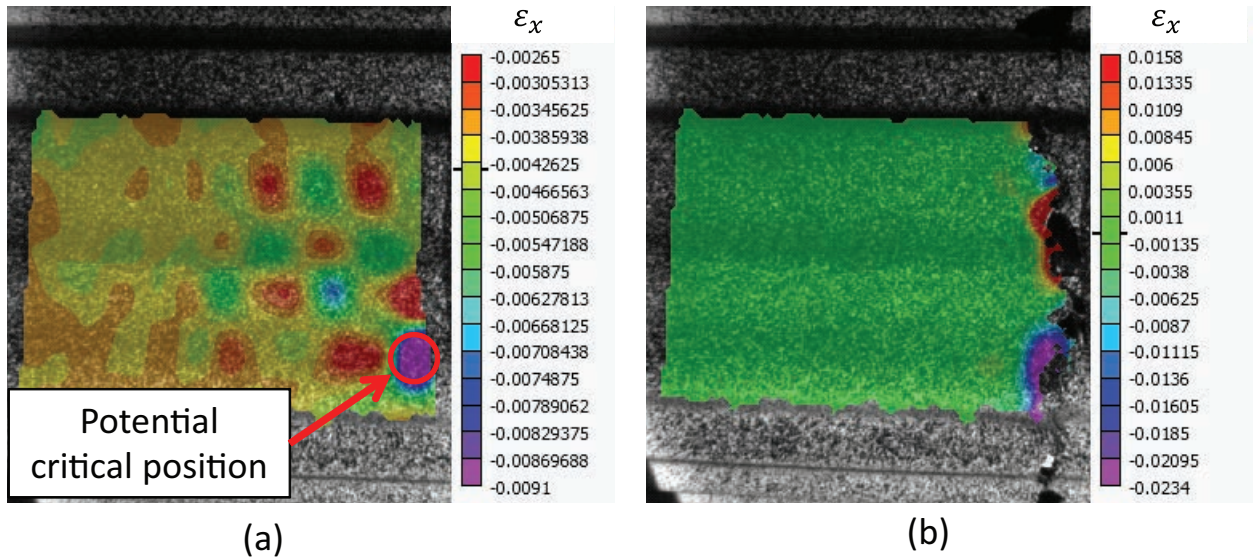


Figure 44: (a) Pre-critical axial strain field of wavy shell 2. The potential critical buckling position are shown in the circle, where the shell thickness is $186 \mu\text{m}$ (b) Postbuckling shape. The crease on buckled shape goes through the potential critical position.

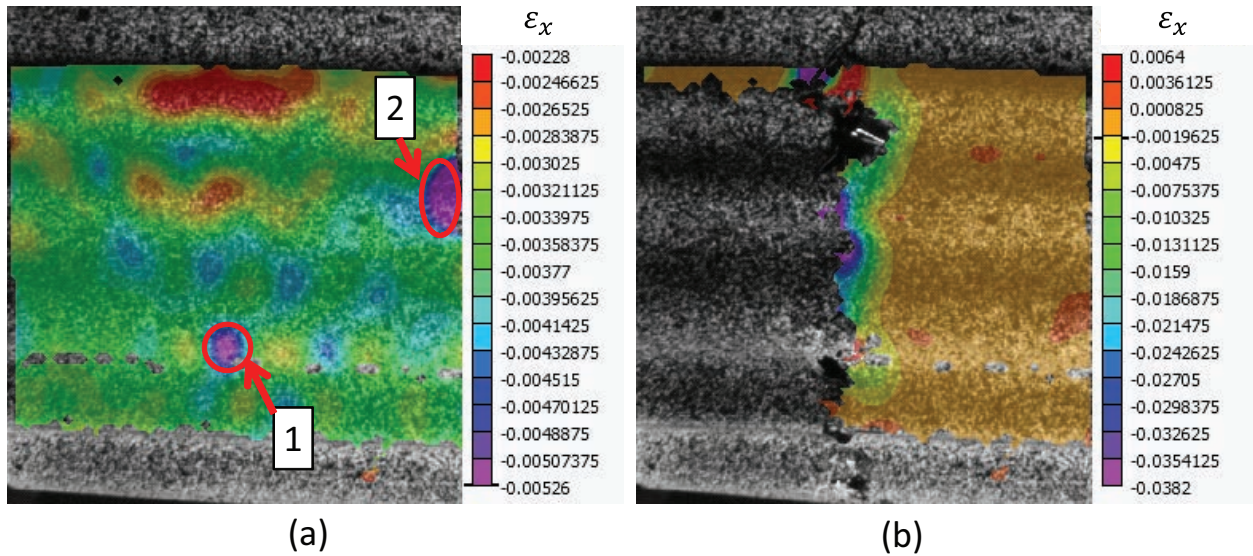


Figure 45: (a) Pre-critical axial strain field of wavy shell 3. The large compressive stains are shown in circles 1 and 2, where the shell thickness is 164 and $187 \mu\text{m}$, respectively. Thus, the potential critical buckling position is in circle 1. (b) Postbuckling shape. The crease on buckled shape goes through the potential critical position.